UNIVERSITY OF CALIFORNIA,

IRVINE

Dual-energy material decomposition and lesion characterization using spectral mammography

THESIS

submitted in partial satisfaction of the requirements

for the degree of

MASTER OF SCIENCE

In Biomedical Engineering

by

Nikita Kumar

Thesis Committee:

Professor Sabee Molloi, Chair

Professor Zhongping Chen

Associate Professor Gultekin Gulsen

2015

DEDICATION

To

My family and friends for being an incredible source of support to me

throughout this journey

TABLE OF CONTENTS

Page

LIST OF FIGURES

LIST OF TABLES

ACKNOWLEDGMENTS

I would like to express my gratitude and appreciation to my committee chair, Professor Sabee Molloi. His support played a significant role in the completion of this project. I would like to thank the members of my committee, Professor Zhongping Chen and Professor Gultekin Gulsen, for volunteering their time for my thesis.

I would also like to thank the following:

Molloi Lab members, past and present:

Dr. Huanjun Ding

Dr. Hyo-Min Cho

Dr. Alfonso Lamng

Dr. Benjamin P Ziemer

Dr. Hanna Javan

Dr. Bahman Sadeghi

David Sennung

Travis Johnson

Luke Higgins

Rachel June Smith

Jerry Lipinski

Logan Hubbard

Others

Philips Healthcare, Sweden

ABSTRACT OF THE THESIS

Dual-energy material decomposition and lesion characterization using spectral mammography

By

Nikita Kumar

Master of Science in Biomedical Engineering

University of California, Irvine, 2015

Professor Sabee Molloi, Chair

Breast cancer is one of the most commonly diagnosed forms of cancer amongst American women. Mammographic density has been strongly associated with breast cancer risk. Previous quantitative assessments of percent density have shown that women with higher percentage of fibroglandular tissue have a higher risk of being diagnosed with breast cancer. It has also been established that mammographic density is associated with higher water and lower fat content in the breast. This implies that women with breasts containing higher volumetric percentage of water and lower percentage of lipid are at a higher risk of developing breast cancer. The ability to quantify water and lipid in the breasts with mammographic images has the potential to stratify women based on breast cancer risk. Thus the purpose of this project was to employ dual-energy material decomposition technique to demonstrate the feasibility of quantifying water and lipid in breast tissue. Calibration study was performed to determine the fitting coefficients in the dual-energy non-linear inverse function to determine material thickness. Postmortem breasts were imaged using a spectral mammography system and dual-energy material decomposition was implemented to quantify water and lipid in the breasts. The results

from mammographic images were compared to results from chemical analysis, the reference standard. The thickness of water and lipid could be measured with RMS errors less than 1mm and density with RMS error less than 1% demonstrating a linear relationship. A high correlation between the two datasets was observed concluding that dual-energy mammography demonstrates the potential for breast cancer risk assessment based on water and lipid content. Suspicious lesions detected during early screening requires the patient to undergo needle biopsy or further imaging examinations to determine the nature of the lesion. However, due to mammography's low specificity for malignant lesions, several healthy women are often recalled for diagnostic procedures. Prior studies have suggested that breast lesion tissue containing higher than normal percentage of water and lower lipid have higher tendency of being malignant. The purpose of this project was also to further extend the application of dual-energy mammography to breast lesion characterization. Dual-energy images of postmortem breasts with lesion phantoms were studied. The measured thicknesses and densities of the lesions were compared to known values and a linear relationship was observed. RMS errors of less than 1mm and less than 10% were calculated for thickness and density respectively. The small errors were indicative of a good match between the measured datasets and the applied fitting function and further emphasized the accuracy of dual-energy mammography in lesion characterization.

CHAPTER 1

Introduction

Background

Breast cancer is one of the most commonly diagnosed forms of cancer amongst American women. The year 2014 has recorded an estimate of 232,670 new cases and death expectancy of about 40,000 women due to breast cancer, although the death rate has been decreasing over the last decade [1].This fall in death rate may be attributed to treatment advances, earlier detection through screening, and increased awareness. The ability to detect breast tumor in its early stages serves as the primary motivation for investigating novel and improvised breast imaging techniques. The imaging techniques currently available clinically include mammography, ultrasound, magnetic resonance imaging (MRI), and radionuclide imaging. Despite some of its minor down falls, mammography is the imaging modality that is currently employed for breast cancer screening due to its imaging capabilities, scan time and reduced cost. However, its effectiveness is reduced in women with dense breasts. Once a lesion has been detected through screening mammography, breast ultrasound is performed to differentiate between cystic and solid masses to aid needle biopsy [2]. In addition to mammography, MRI may be performed which provides higher sensitivity but lower specificity and higher cost [2]. Single-photon emission computed tomography (SPECT), positron emission mammography (PEM), positron emission tomography (PET) and scinti-mammography are imaging modalities that employ radionuclide and used for diagnostic purposes.

While there have been considerable advances in mammography, there is one major limitation of reducing the three-dimensional anatomy of the breast into a two-dimensional image. This superposition of the breast tissue masks the underlying anatomical information and impairs lesion detection. In addition, tissue superposition can create a false impression of a lesion's existence, thereby resulting in subjects being recalled unnecessarily for needle biopsies and additional radiation based imaging. This motivated investigators to develop techniques that provided depth information in breast x-ray imaging. Currently, stereoscopic digital mammography (SDM), digital breast tomosynthesis (DBT), and dedicated breast computed tomography (BCT) are three modalities that are being actively investigated. However, these imaging techniques have their limitations as well. DBT relies on acquisition of multiple projection views over a limited angular range to reconstruct a volumetric image. This results in good separation in anatomical data but with considerable loss of spatial resolution along the depth-direction due to limited angular sampling causing concern about its ability to detect subtle structures. BCT provides excellent anatomical details and lesion visualization without the need for compression but provides limited breast coverage.SDM on the other hand, reduces false-positives by 39% and false-negative by 46%, but requires twice the amount of dose [2].Contrast enhanced X-ray imaging is considered as an adjunct technique showing some promising aspects in terms of tumor staging and identifying tumor extent for breast conservative surgery. However, these techniques require intravenous injection, which elevates risk [3].

Significance

This study proposes a low-dose spectral mammography technique to assess breast cancer risk and further characterize the nature of the detected breast lesion in terms of its water and lipid contents. The proposed technique is expected to improve the positive predictive values and reduce the number of false-positive results without additional radiation dose. The innovation is in employing a photon-counting, energy resolving, multi-slit Si-strip detector based mammography system. This system has the ability to record the energy of individual photons interacting with the detector thereby making dual-energy material decomposition in terms of water and lipid possible. Recent reports have suggested a positive correlation between increased tissue water content and carcinogenesis [4]. It has been suggested that increased cell water content not only promotes cell division and oncogene expression, but also accelerates cells' respiration rate, which enhances their ability to compete for nutrients with normal cells [5] and that the degree of malignancy increases with the degree of cell hydration [6]. These reports suggest that breast cancer risk may be assessed by quantifying water and lipid content in the breasts. Other investigations have reported that malignant tumors have reduced lipid (∼20%) and increased water (>50%) contents compared to normal breast tissue [7, 8]. If lesions could be characterized quantitatively according to their chemical compositions, predictive capability might be improved. It has also been reported that 60% of women undergoing mammographic screening annually over a decade have a false-positive result [9].This high number of false-positive results is of concern since it would subject many women to unnecessary biopsies and other follow-up examinations. Thus, there is increased interest in developing lesion characterization technique that can characterize circular lesions as benign or

malignant during the initial screening. These reports indicate that mammography's sensitivity and specificity may be improved if breast tissue composition can be accurately measured, in order to better characterize lesions according to their composition.

Through this project an innovative technique has been presented which enables stratifying patients according to breast cancer risk. The technique is based on breast material decomposition to quantify water and lipid present in the breast. Previous studies have reported that women with dense breasts are more susceptible to breast cancer. Breast tissue encompasses fibroglandular tissue and fatty tissue. Higher percentages of fibroglandular tissue make the breasts dense. This tissue contains higher percentage of water compared to fatty tissue. Thus it can be established that breasts with high water content are at higher risk of developing breast cancer. This study employed dual-energy material decomposition spectral mammography to quantify water and lipid content in breasts to assess breast cancer risk. The survival rate amongst the women diagnosed with cancer greatly depends on the stage of cancer detected making it crucial to detect cancer in its infancy. The dual-energy material decomposition technique is further applied to quantify water and lipid in detected lesions to predict their potential malignancy.

Specific Aims

This project proposes a material decomposition technique to quantify water and lipid in breast tissue and in breast lesions for cancer risk assessment and lesion characterization. The technique uses a spectral mammography system based on multi-slit Si-strip photon-counting detectors. This system which has recently been clinically introduced provides spectral image

data in addition to the standard screening mammogram without any additional radiation exposure. The central hypothesis of this study is that the water and lipid contents of malignant tissue differ from those of normal tissue. The proposed technique is expected to reduce the number of false positive results in breast lesion diagnosis. The specific aims of this project are:

I. Investigate the hypothesis that spectral mammography can be used to measure water and lipid contents in phantoms

II. Investigate the hypothesis that water and lipid contents of breast tissue can be accurately measured using postmortem breasts and chemical analysis as the reference standard

III. Investigate the hypothesis that water and lipid content can be accurately measured in lesion phantoms inserted in postmortem breasts

Overview

Following this chapter on introduction to the project is a chapter on basic principles of X-ray imaging and mammography. Chapter 3 contains information about the features and technological innovations in the mammography system employed during the study. A calibration study was performed to obtain coefficients for dual-energy material decomposition with plastic water and adipose-equivalent materials as basis. The details of this study are described in chapter 4. The coefficients developed in chapter 4 for adipose and plastic water are converted to lipid and water respectively. These conversion factors are developed through a calibration study with details presented in chapter 5. This chapter also describes a postmortem breast study to quantify water and lipid in the breast tissue by applying the

calculated conversion factors. Chapter 6 presents a lesion characterization study using lesion phantom disks inserted in postmortem breasts. The thesis ends with a summary and suggestions for future work.

CHAPTER 2

Conceptual background

2.1. X-ray basics

X-rays are electromagnetic radiations with photons having energies between 100 eV and 100 keV. X rays can penetrate some substances more easily than others. The ability of X-rays to penetrate depends not only on their wavelength, but also on the density and thickness of the substance. Due to their penetrating ability, they are used for medical imaging purposes. Mammography is one such imaging modality that utilizes X-rays.

2.1.1. Generation of X-rays

X-rays are produced by accelerating electrons with high voltage and letting them collide with a metal target. The electrons decelerate on colliding with the metal target and thus produce X-rays. This is called Brehmsstrahlung radiation. (Figure 1) Some of the incoming electrons could also generate X-rays in a different manner when they knock out an inner shell electron of an atom of the anode. The vacancy created is then filled by an outer shell electron that releases the energy difference through generation of high energy photons. These are called the characteristic X-rays and specific to the anode material.

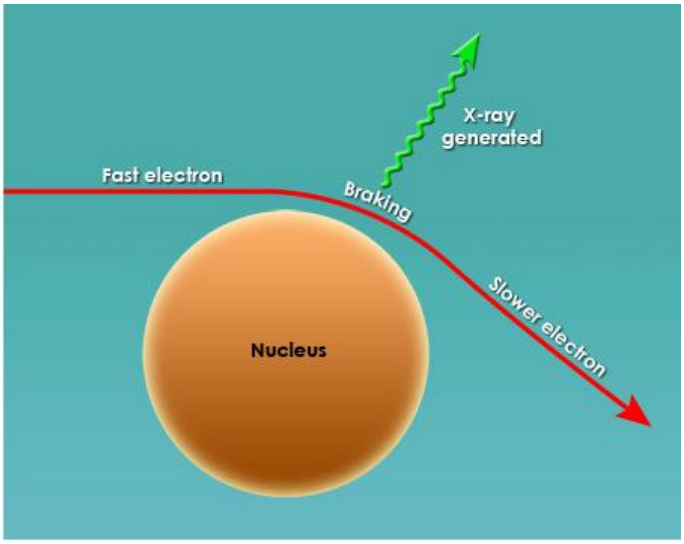

Figure 1: X-ray generation

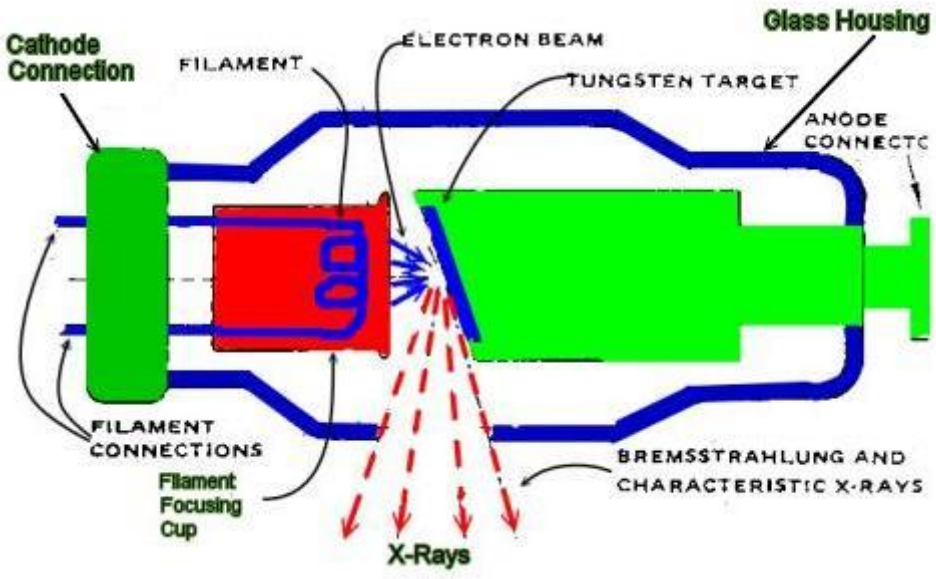

Figure 2: X-ray tube

X- ray tube and X-ray generator are the necessary components for X-ray production. (Figure 2)The X-ray tube provides the required environment for X-ray production and the X-ray generator provides the source of electrical voltage. In the x-ray tube, two electrodes, the

cathode and anode, are situated a small distance apart. Connected to the cathode and the anode are negative and positive high voltage cables, respectively, from the x-ray generator. A small increase in the filament voltage results in a large rise in tube current that accelerates electrons from the negative cathode to the positive tungsten anode target. The anode rotates to dissipate heat and X-ray beam is emitted. The generated X-ray spectrum has the appearance as shown in (Figure 3)

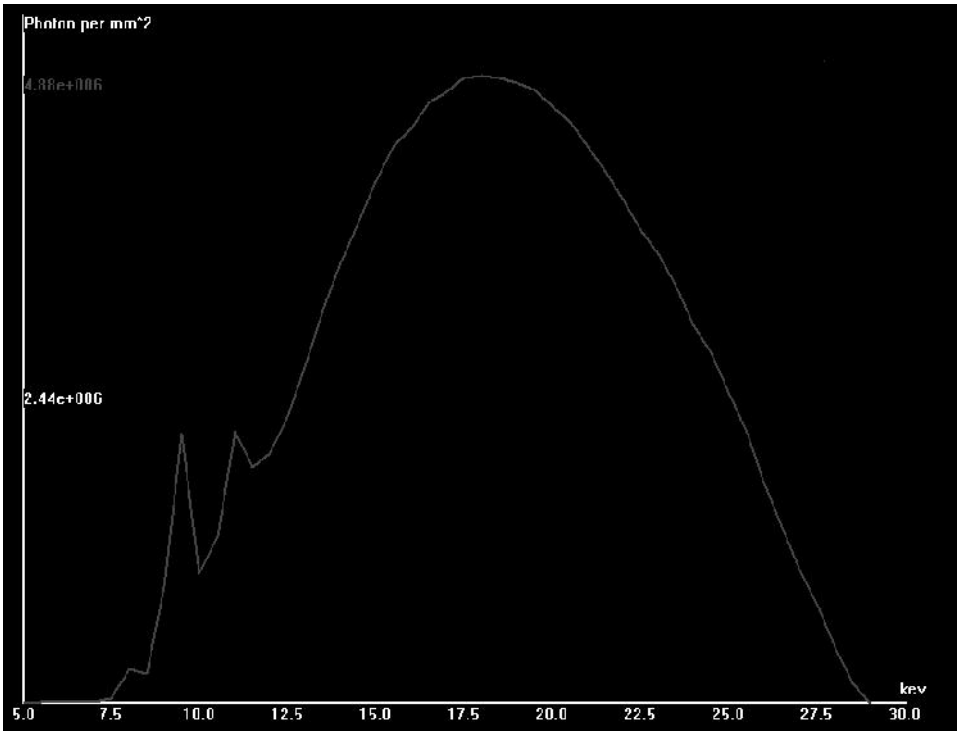

Figure 3: X-ray spectrum for tube voltage of 29kVp using 0.40mm Al-filter and 0.76mm Be-filter

2.1.2. Interaction of X-ray with matter

X-rays when exposed to a material, interacts with matter in three forms:

(i) Photoelectric absorption

In a photoelectric interaction, the incoming X-ray knocks an electron out of an inner (K-shell or L-shell) orbital of the atom (Figure 4) and much of the energy of the X-ray is transferred to this photoelectron. When the vacancy is refilled by an electron from a more loosely bound shell, the remainder of the energy is transferred either to a second (Auger) electron or to a relatively low-energy fluorescent X-ray.

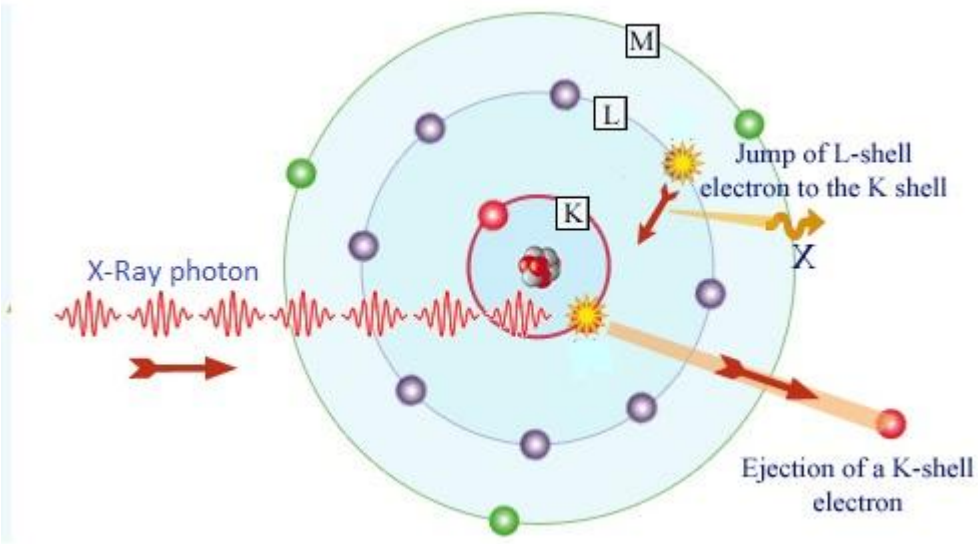

Figure 4: X-ray photon interaction resulting in photoelectric absorption

(ii) Compton scatter

Compton scatter results in a part of the energy of the incoming X-ray being absorbed at the initial point of X-ray impact resulting in the liberation an energetic recoil electron. The remaining energy is carried away by the scattered quantum to be deposited elsewhere,

resulting in the loss of spatial resolution. The probability of occurrence of Compton scattering increases with increase in X-ray energy.

(iii) Rayleigh scatter

X-ray photon interacts with the whole atom and is scattered without change in its own energy or the internal energy of the scattering atom. The scatter occurs mainly in the forward direction.

When X-rays propagate through a material, some of the photons are lost due to scatter. This loss of photons is termed as attenuation and it is dependent on the density of the material. Higher density materials attenuate to greater extents. When applied to medical imaging, different anatomical structures attenuate differently and this is represented through different levels of contrast. Structures that attenuate highest appear white while those that attenuate least appear dark.

The number of photons *N(x)* transmitted through a material of thickness *t* can be expressed as:

$$N(x) = N_o(x)e^{-\mu(x)t}$$

Where $N_o(x)$is the number of photons incident on the material, μis the linear attenuation coefficient of the material usually represented with the unit cm^{-1}. The three terms are dependent on X-ray energy *(x)*. A material with higher attenuation coefficient allows fewer photons to pass through it.

2.2. Mammography

Mammography is the process of using low-energy X-rays (around 30 kVp) to examine the human breast, which is used as a screening and diagnostic tool. The goal of mammography is the early detection of breast cancer, typically through detection of characteristic masses.

Screening mammography, however, has a few disadvantages. Firstly, false-positive results often occur wherein radiologists express the presence of a lesion while actually the mammogram is normal. All abnormal mammograms are followed up with additional testing (diagnostic mammograms, ultrasound, and/or biopsy) to determine the presence or absence of cancer. False-positive mammogram results can lead to anxiety and other forms of psychological distress in affected women. The additional testing required to rule out cancer can be expensive, time consuming and may cause physical discomfort.

Secondly, screening mammograms have the ability to detect forms of cancers that are not life threatening in addition to cancers that need to be treated. This often leads to "overdiagnosis" of breast cancer. Overtreatment exposes women unnecessarily to the adverse effects associated with cancer therapy.

Lastly, false-negative results occur when mammograms appear normal even though breast cancer is present. Overall, screening mammograms miss about 20 percent of breast cancers that are present at the time of screening. The main cause of false-negative results is high breast density. Breasts contain fibroglandular and adipose tissues. Because fibroglandular tissue and tumors have similar density, tumors can be harder to detect in women with dense breasts. False-negative results can lead to delays in treatment and a false sense of security among affected women.

2.2.1. Digital Mammography

Digital mammography system is one in which the x-ray film is replaced by solid-state detectors that convert x-rays into charge/electrical signals in the detector. The electrical signals are used to produce images of the breast that can be seen on a computer screen or printed on special film similar to conventional mammograms.

2.2.2. Detectors

The conventional screen-film mammography systems used intensifying screens made of rare earth phosphors to capture X-rays. But, due to the trade-off between sensitivity and resolution, screen-films are replaced by detectors in digital mammography systems. Employing digital technology offers several advantages to mammography. Digitizing images allows easy electronic transfer and storage without the need for physical storage. There are two types of digital detector technologies: indirect and direct photon detectors. Indirect digital detectors convert the incoming X-ray photons into visible light which is captured by either photodiodes or CCDs and converted into electrical signals. In the direct photon detection technology the incoming X-ray photons are completely absorbed by the detector material and the interaction results in production of charge that is proportional to the energy of the interacting photon. These detectors are made of materials of high atomic number in order to absorb the incoming high energy X-ray photons.

Charge-integrating detectors

The charge created from the incoming X-ray photons can be summed at each pixel and the integrated energy at that pixel is recorded. These detectors are not capable of energy resolution and swank noise can be a serious cause of image degradation. This noise is introduced by the statistical variation of released light after the conversion of the photon. Hence, two photons of the same energy can have different responses in the detector which translates to an overall uncertainty in the integrated signal.

Photon-counting detectors

Photon-counting detectors count the number of electrical pulses that are above a specified threshold. Incoming x-ray photons deposit energy at the photon counting detector, thereby generating electrical charges. The charges then travel within the detector under the influence of the electric field toward the electrodes and induce a pulse signal, which is then processed by the Application Specific Integrating Circuit (ASIC) [10]. The height of the induced pulse is compared with a specified energy threshold value using a comparator. A count is registered in the counter if the pulse height exceeds the threshold value. On subtracting counts in counters from adjacent energy thresholds the counts in the energy bin defined by the two thresholds are obtained.

The photon-counting detector has several advantages over the charge-integrating detectors. Firstly, the photon-counting detectors can eliminate electronic noise. Secondly, the energy resolving property of the detector provides the capability of varying the contribution of photons to the overall signal. By knowing their energy, photons can be weighted differently to produce images of optimal contrast-to-noise ratio, unlike the charge-integrating detector,

wherein the low energy photons that contribute most to the contrast are weighted less [10, 11].

2.2.3. Dual energy mammography

Dual energy subtraction is used in digital mammography to exploit differences between the effective atomic numbers of different tissues. Adipose and glandular tissues have effective atomic numbers of 6.33 and 6.93, respectively [12]. The attenuation of low-energy X-rays is highly dependent on Z due to Z^3 dependence of photoelectric effect which is a dominant form of X-ray interaction at low-energies of X-ray. At higher energies, however, Compton interaction dominates and is less dependent on Z and more dependent on the physical density. Contrast on mammographic images changes with X-ray energy and the amount of change depends on the effective atomic number of the tissue material.

Dual energy mammography requires the acquisition of a mammographic projection image at low- and high-energy. This is achieved through two X-ray exposures at two different tube voltages (kVp). The two images (I_1 and I_2) are subjected to weighted logarithmic subtraction, where R is the weighting factor

$$ln(I_1)\text{-}R\ ln(I_2)$$

By adjusting the value of R, a suitable level of contrast between the two tissues can be attained. Dual energy capability is available on clinical mammography systems.

2.2.4. Spectral mammography

Spectral mammography is a new technique where the energy of each photon is utilized in the color representation of the breast based on energy levels corresponding to breast tissue composition [13]. The photon-counting technology with its ability to count the number of incoming photons based on their energies provides the additional benefit of generating these colored X-ray images. Previous studies have demonstrated that in 23% of the cases, the conventional X-ray images underestimate the stage of the tumor compared to the color X-ray with energy discrimination capability [14]. Spectral imaging depends on a reliable measurement of the energy-dependent attenuation coefficient for different materials. Essentially, color X-ray images have the capability to sort tissue or materials based on their chemical composition. As X-ray spectral absorption depends largely on the element's atomic number, the examination of the absorbed or transmitted spectrum provides information on the relative concentration of the elements. The photon-counting detector classifies the incoming photons into two energy bins based on their energies. Two thresholds are specified, one for the low energy photons and the other for high energy photons. Since the lower energy photons contribute most towards contrast, equal weighting is assigned to both low and high energy photons. The resulting image provides a clear distinction between different tissues/materials. Spectral imaging provides visual aid in quantifying water and lipid in the breasts. This plays a vital role in stratifying patients for breast cancer risk based on the percentages of water and lipid in the breasts.

CHAPTER 3

The MicroDose mammography system

3.1. Introduction

The Philips MicroDose SI is a scanning multi-slit photon-counting mammography system. It is the first single-shot full-field digital mammography system capable of non-invasive, spectral imaging without the need for contrast injection.

3.2. System description

The system set up for the MicroDose SI is shown in figure 5. X-rays are produced from a tungsten anode X-ray tube and subjected to filtration by a 0.40mm Al-filter and 0.76mm Be-filter. The filters help in eliminating the low-energy photons that would increase the dose without contributing towards the image. The beam is then subjected to collimation by pre-collimator that splits the X-ray beam into smaller beams to match the post-collimator and the detector. The X-ray beam passes through the compression paddle that is used to compress the breast during image acquisition. Post-collimators are located before the detector so as to eliminate the scattered radiation from the tissue. The detector is placed perpendicular to the chest wall(Y-direction). Both the detector and the collimators are mounted rigidly and scans are performed parallel to the chest wall (X-direction). Thus 2D projection images are obtained.

3.2.1. X-Ray tube

In this system, the X-ray tube consists of tungsten anode. Tungsten does not have characteristic lines in the mammographic energy range thus making it a favorable choice of anode material. It enables easy manipulation of mean energy in the produced X-ray spectrum. The system has a focal spot of 0.3mm and the tube is operated at 26, 29, 32, 35 and 38kVp giving the corresponding maximum energy of the photons in keV.

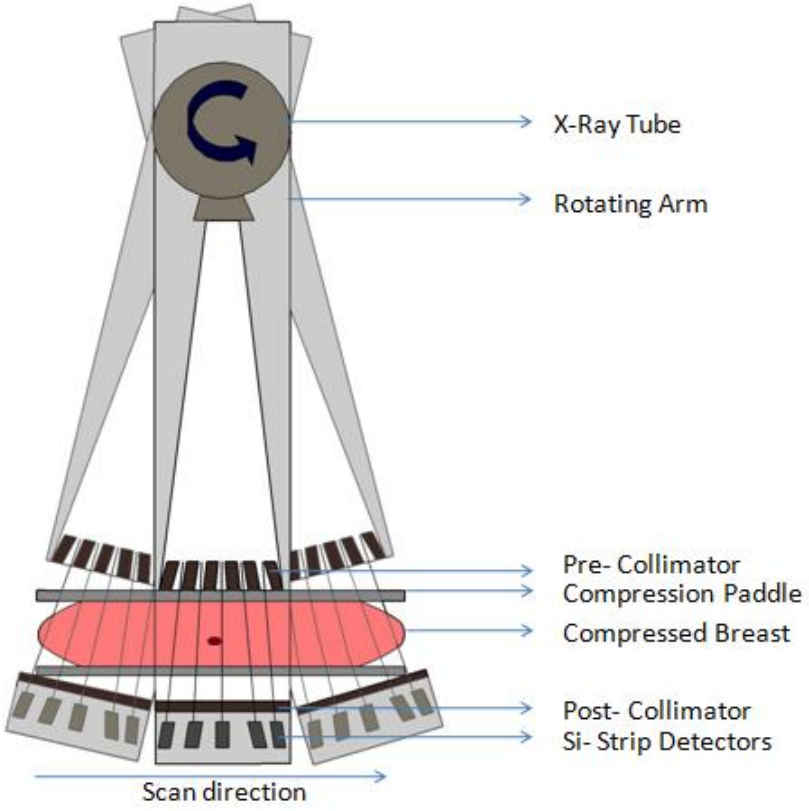

Figure 5: MicroDose SI system setup

3.2.2. Detector design

The detector system consists of a large number of crystalline silicon strip detectors. Silicon is preferred due to its electronic properties and good energy resolution. However, due to its low atomic number (Z=14) Si does not have the ability to attenuate the incoming high energy photons. This is overcome by implementing the edge-on silicon strip geometry where the long axis of the silicon strip detectors are placed parallel to the direction of the X-ray beam, shown in figure 6. This creates sufficient absorption length and improves the detector quantum efficiency in the mammographic energy range.

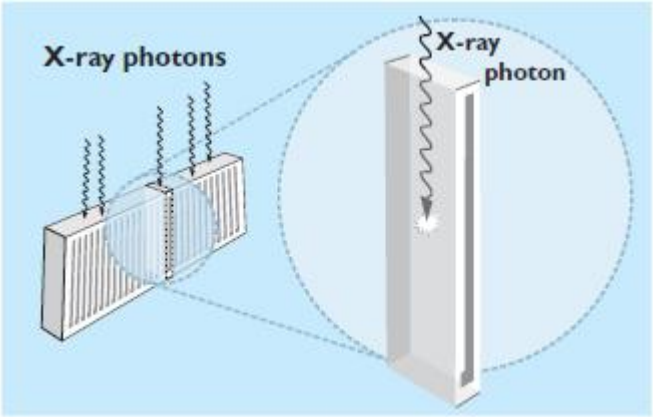

Figure 6: Edge-on silicon strip geometry

Every X-ray photon incident on the detector interacts with the Si to produce several thousands of electron-hole pairs without the need for amplification. A bias voltage is applied across the detector, which generates an electrical field causing oppositely charged charge-clouds to move towards to the corresponding electrodes. This drift induces a short electrical signal on the

electrodes. The generated signal is subjected to pulse shaping using suitable electronics, shown in figure 7.

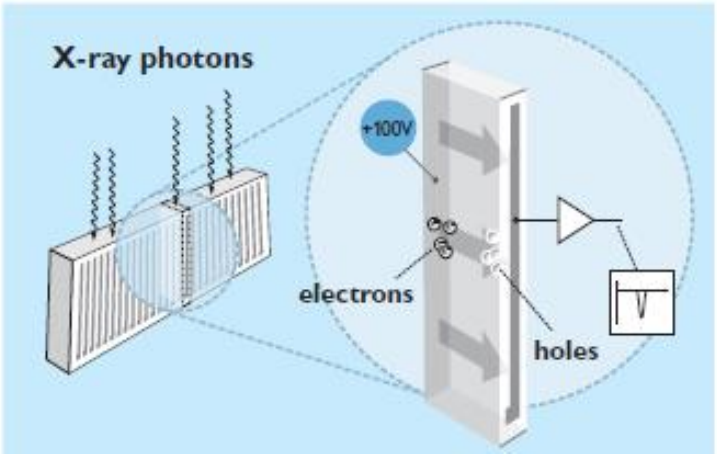

Figure 7: Conversion of X-ray photon energy to electrical signal

The detector system is supported by custom designed ASIC (Application Specific Integrated Circuit) that consists of several components like the preamplifier, pulse-shaper, comparator and digital counter .There are multiple channels in the ASIC and they function in parallel. The pulse-shaper generates a signal around a few hundred nanoseconds in duration. The comparator discriminates pulses that are above a certain threshold level from the detector noise (figure 8). The 15 bits dynamic counter counts the pulses that are found to be above the specified threshold. Each ASIC read-out channel can handle count rates up to 2 MHz, thus being able to acquire images with exposures lasting as short as 3-15seconds. .The number of counted photons in each channel is accumulated during a single sampling interval and then subjected to image reconstruction. The incident pulse is an order of magnitude higher than the noise level

allowing the detector to easily distinguish between noise and the pulse due to the incident photon. Thus the detector only counts the number of pulse peaks.

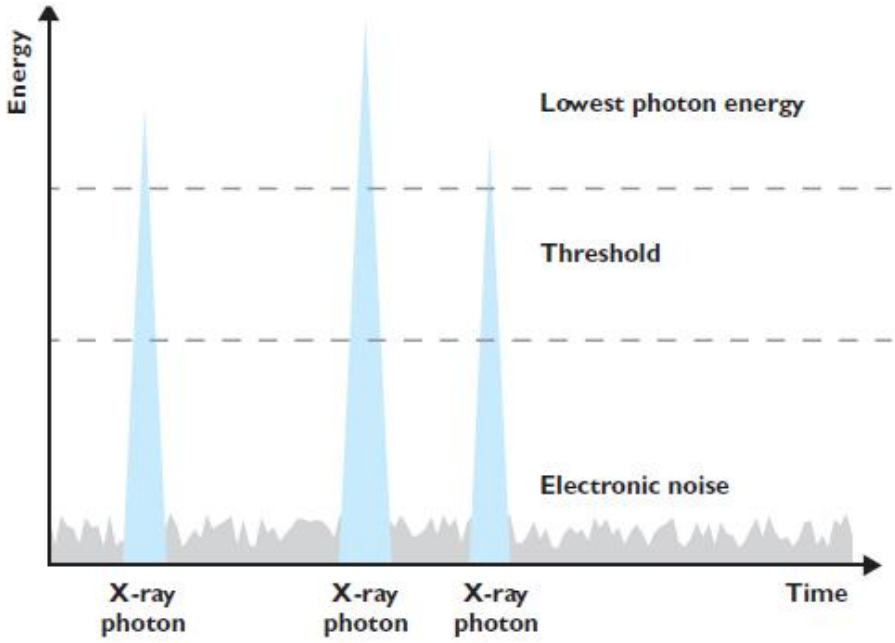

Figure 8: Selection of optimum energy thresholds

Two thresholds are employed, one to eliminate noise and another to divide the incoming photons into low and high energy bins. The energy thresholds are selected so as to provide a quantum efficiency of about 90%.

The energy weighting scheme applied to the detected photon energies in this system is different from that applied in the commercial charge-integrating type mammography systems. As the photons passing through the breasts interact with the detector the charge produced is proportional to the photon energy. The attenuation and contrast depend on the energy of the photons and it is the lower energy photons that contribute most of the contrast information. In

charge-integrating detectors the energy weighting is proportional to the photon energy due to which the lower energy photons are weighted less. In the photon-counting detectors however, all photons are weighted equally preventing the loss of information. Thus the photon-counting detector is an improvement over the charge-integrating type. This technology also improves dose efficiency by 10% [15].

3.2.3. Multi-slit scanning technology

The photons pass through a pre-collimator placed above the breast and a post-collimator placed between the breast and the detector. The multi-slit collimators shape the beam to match the detector, and a two-dimensional image is generated when beam and detector are scanned relative to the breast.

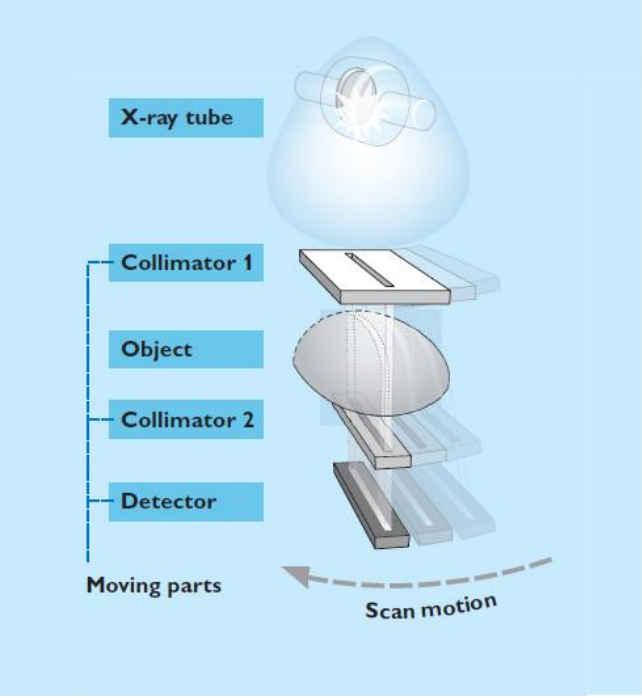

Figure 9: Scanning multi-slit geometry

The slits, shown in figure 9, created by the combination of the pre- and post- collimators are lined up with each of the Si detector strips. The pre-collimator removes the photons that are not directed towards the detector. The post-collimator absorbs the photons scattered by the breast and not directed towards the detector. This technique overcomes the major limitation of scattered radiation faced by flat-panel detectors. During the continuous scan the detector is read every 2ms.

CHAPTER 4

Dual-energy material decomposition using spectral mammography: A calibration study

Abstract

Purpose

To investigate the feasibility of quantification of breast tissue chemical composition with dual-energy mammography through phantom study

Methods

Phantom images were acquired using a Si-strip based photon counting mammography system. The system was calibrated for dual-energy material decomposition using plastic water and adipose-equivalent phantom. The phantom was designed to have varying densities of plastic water and adipose (0, 25, 50, 75, 100%) at different thicknesses (2, 4, 6, 8 cm). Low- and high-energy images were acquired at different tube voltages (26, 29, not 32, 35, 38kVp). Rectangular ROIs were drawn within each block of the calibration phantom in the images and corresponding attenuation coefficients were measured. Calibration coefficients were calculated using the low- and high-energy log signals and the known thicknesses of plastic water and adipose in the calibration phantom for different tube voltages. The estimated coefficients were then applied to calculate the density of the two materials in the phantom as a validation procedure.

Results

Fitting coefficients were estimated for plastic water and adipose at 26, 29, 32, 35 and 38kVp. Known and measured thicknesses and densities were compared respectively. Relative error in measured thickness and density for each of the 20 calibration points were observed. The RMS error in thickness of plastic water and adipose were found to less than 1mm. The RMS error in density was calculated to be less than 1% at all tube voltages.

Conclusion

The small errors are indicative of a good match between the non-linear fitting function for dual-energy calibration and the acquired data.

4.1. Introduction

Mammographic density has been strongly associated with breast cancer risk [16, 17]. Breast tissue mainly consists of fat and fibroglandular tissue. Radiologically, fat having a lower x-ray attenuation coefficient than fibroglandular tissue, appears dark on a radiographic image. The bright regions however, characterize stromal and epithelial tissue and are referred to as mammographic density [18]. Previous quantitative assessments of percent density have shown that women with higher percentage of fibroglandular tissue, occupying ≥ 75% of the total breast area have a 4 to 6 fold higher risk of being diagnosed with breast cancer than women with < 10% [19]. It has also been established that mammographic density is associated with higher water and lower fat content in the breast. Thus breasts with higher volumetric percentage of water and lower volumetric percentage of lipid are at a higher risk of developing breast cancer. Furthermore, several reports have suggested that breast lesion tissue containing

high percentages of water and lower lipid content have higher tendency of malignancy. The ability to quantify water and lipid in breast tissue and detected breast lesions through mammographic images could further reduce the deaths due to breast cancer by ensuring early diagnosis and treatment. Characterization of lesions during the initial screening could lower the number of false-positive cases and potentially reduce the number of patients being recalled for further examination.

This project presents a technique to quantify two basis materials using dual-energy spectral mammography by means of a phantom study. The basis materials under consideration were plastic water and adipose-equivalent plastic since liquid water and lipid cause inconvenience in handling. The principles of dual-energy material decomposition were employed in quantifying the density of plastic water and adipose-equivalent plastic phantoms and obtaining the calibration coefficients. These coefficients were then later employed to quantify density of lesion phantom disks inserted in the postmortem breasts.

4.2. Dual-energy decomposition

Low- and high-energy images can be combined to enhance certain components in an X-ray projection image. However, linear log-subtraction applied in this process to obtain quantitative dual-energy images can be affected by the presence of the non-linear scatter and beam-hardening effects. Thus, non-linear inverse functions were applied to obtain the thickness of the materials from the log-signals. A non-linear function with twelve coefficients ($a_0, a_1, a_2 \ldots$) was employed for the calibration procedure.

$$T = \frac{a_0 + a_1 x + a_2 y + a_3 x^2 + a_4 xy + a_5 y^2 + a_6 x^3 + a_9 y^3}{1 + b_1 x + b_2 y + b_3 x^2 + b_4 xy + b_5 y^2}$$

The thickness *T* of each of plastic water and adipose-equivalent plastic was fit individually to the low- and high-energy log-signals (*x* and *y* respectively) using non-linear least-squares minimization algorithm [20, 21, 22]. Figure 10 shows the low-energy log-signal images for different thicknesses of plastic water and adipose.

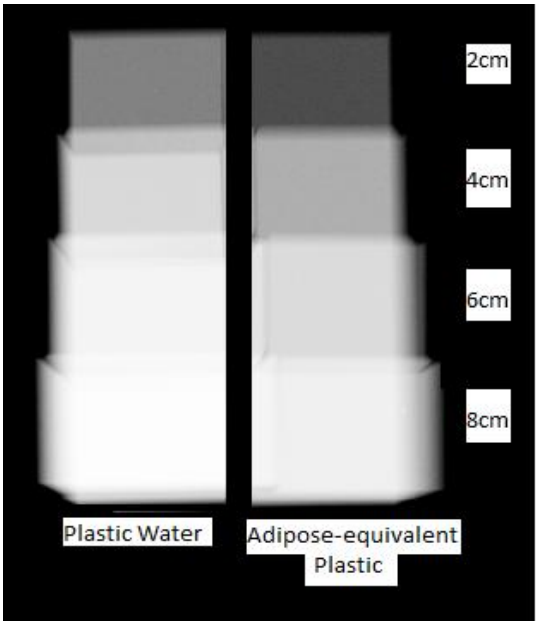

Figure 10: Low-energy image of plastic water and adipose of different thickness

Due to the polyenergetic nature of diagnostic X-ray, and the characteristic dependence of linear attenuation coefficient on energy, low- and high-energy images of this phantom was obtained at different tube voltages (26, 29, 32, 35, 38 kVp).Thus a set of calibration coefficients were obtained for each of plastic water and adipose at these tube voltages.

4.3. Materials and methods

4.3.1. Calibration phantom

This study was carried out using plastic water and adipose-equivalent phantom (CIRS, Norfolk, VA). In theory, the system calibration may be performed with pure water and oil. However, both of these basis materials are in liquid form making it challenging for eventual clinical implementations. Plastic water was made to have attenuation similar to pure water and adipose-equivalent plastic mimics the attenuation of 15% water and 85% lipid. Tables 1 and 2 show the chemical composition of plastic water and adipose compared to real water and lipid respectively.

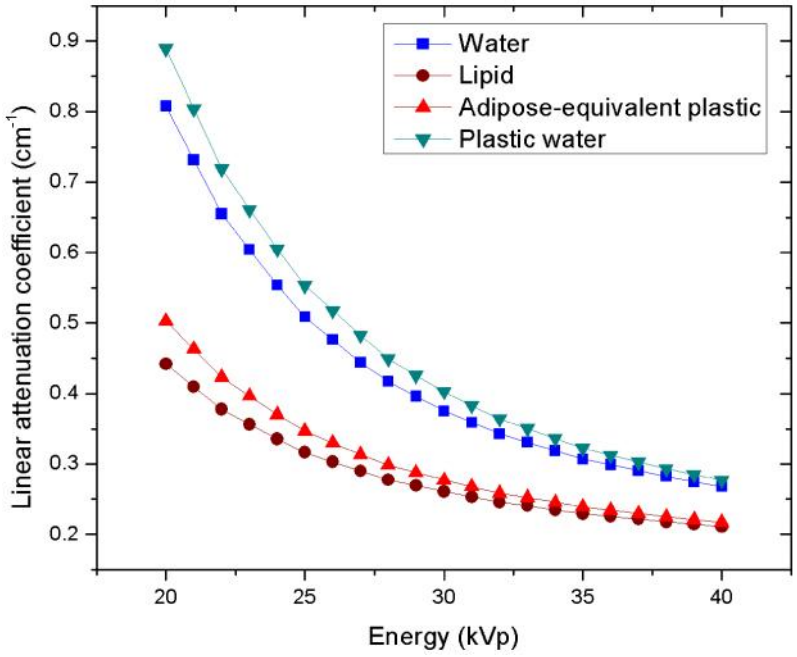

Figure 11: Comparing the linear attenuation coefficients of water and lipid to plastic water and adipose-equivalent material respectively

Table 1: Chemical composition of plastic water and real water

Elements	Mass fraction	
	Water	Plastic Water
H	1.119E-01	8.100E-02
C		6.720E-01
N		2.400E-02
O	8.881E-01	1.990E-01
Cl		1.000E-02
Ca		2.300E-02

Table 2: Chemical composition of adipose and lipid

Elements	Mass fraction	
	Lipid	CIRS Adipose
H	0.118	0.098
C	0.774	0.714
N	0.108	0.020
O		0.163
Cl		0.003
Ca		0.001

The calibration phantom was designed to have different densities (0, 25, 50, 75, 100%) of plastic water and adipose at different thicknesses (2, 4, 6, 8 cm). Different densities were achieved by stacking different thickness combinations of plastic water and adipose. Figure 12 shows the design of the calibration phantom employed in this stage of the project.

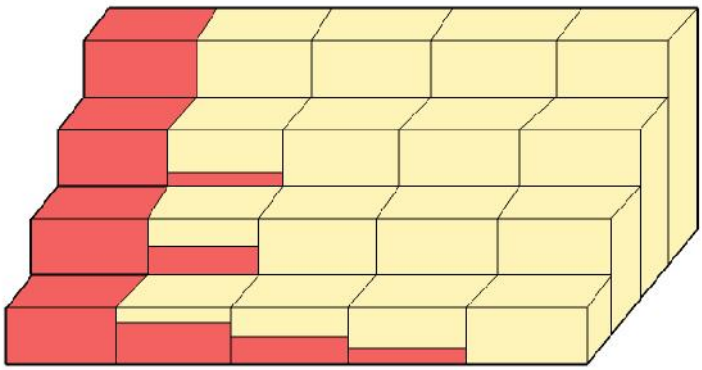

Figure12: Calibration step phantom with 0-100% plastic water (yellow) and adipose (red) of different thicknesses

4.3.2. Image acquisition and processing

The calibration phantom was imaged at different tube voltages (26, 29, 32, 35, 38kVp) and 14mAs using a dual-energy mammography system (MicroDose SI, Philips).High- and sum-energy images were acquired. Low-energy images were obtained by the subtraction of high-energy images from the corresponding sum-energy images. Log-signal images (μt) for low- and high- energy images (I) were obtained by the application of Beer-Lambert equation using the corresponding energy open-field images (I_o).

$$\mu t = -log\left({}^{I}/_{Io}\right)$$

All image processing steps were carried out in ImageJ.

4.4. Calibration procedure

The calibration procedure was carried out using the above described step phantom. Twenty points were selected for dual-energy calibration. The calibration data included plastic water and adipose at four different total thicknesses (2, 4, 6, 8 cm) at five different densities (0, 25, 50, 75, 100%). The calibration dataset is shown in Table 3.

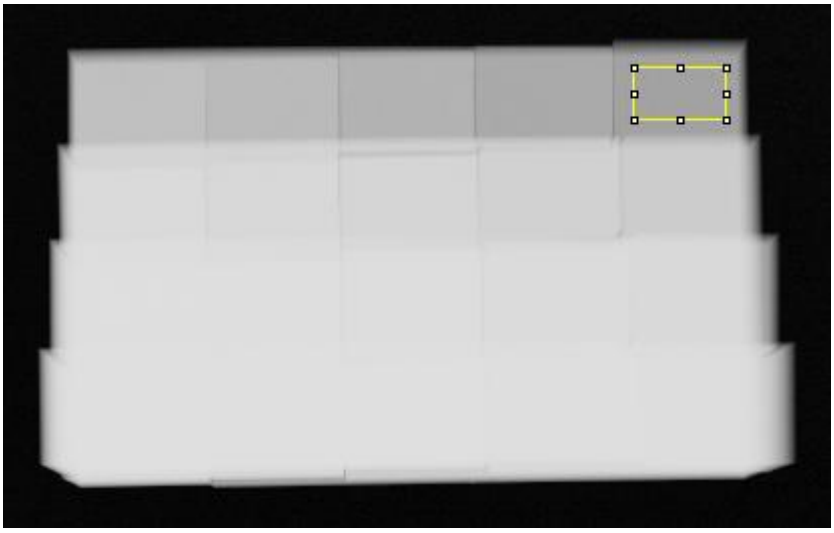

Figure 13: Thickness image of calibration step phantom with ROI (yellow)

4.4.1. Dual-energy thickness measurement

After dual-energy decomposition, the low- and high-energy images yielded plastic water and adipose thickness images. Within these images, suitable rectangular (Region of interest) ROIs were drawn (figure 13) to encompass each of the combinations of thickness and density of two materials in the phantom.

4.4.2. Error analysis

The RMS error (RMSE) in measured density was calculated using the following equation:

$$RMSE = \frac{1}{\sqrt{n}} \sqrt{\sum_{i=1}^{n} (D_m - D_k)^2}$$

Table 3: Thickness and density calibration points for the calibration step phantom

Calibration Point	Total thickness	Known density	Adipose known thickness	Plastic water known thickness
1	2	100	0	2
2	4	100	0	4
3	6	100	0	6
4	8	100	0	8
5	2	75	0.5	1.5
6	4	75	1	3
7	6	75	1.5	4.5
8	8	75	2	6
9	2	50	1	1
10	4	50	2	2
11	6	50	3	3
12	8	50	4	4
13	2	25	1.5	0.5
14	4	25	3	1
15	6	25	4.5	1.5
16	8	25	6	2
17	2	0	2	0
18	4	0	4	0
19	6	0	6	0
20	8	0	8	0

4.6. Results

4.6.1 Dual-energy calibration

The fitting calibration coefficients obtained at different tube voltages are shown in table 4

Table 4: Calibration coefficients for adipose and plastic water at all tube voltages

Coefficient	26kVp		29kVp		32kVp		35kVp		38kVp	
Index	Adipose	Plastic water	Adipose	Plastic water	Adipose	Plastic water	Adipose	Plastic water	Adipose	Plastic water
a0	-1.088	0.727	-1.102	0.783	-2.458	1.477	-3.532	2.424	-1.781	1.088
a1	-20.065	13.365	-20.117	13.144	-26.066	14.857	-24.492	16.122	-29.629	18.099
a2	30.329	-18.912	28.469	-17.487	37.165	-19.771	29.956	-21.457	35.744	-20.005
a3	0.651	-0.756	-1.531	-0.874	-17.821	-0.826	74.588	-12.442	-39.119	18.262
a4	-0.133	0.351	1.199	1.660	53.228	-1.053	213.087	27.211	105.026	-47.659
a5	-2.354	1.404	2.025	-1.004	-38.906	2.491	156.401	-14.542	-66.208	28.742
a6	0.066	-0.028	-0.074	0.091	-0.202	0.151	-0.914	0.438	0.134	0.020
a7	0.000	0.000	0.000	0.000	0.000	0.000	0.000	0.000	0.000	0.000
a8	0.000	0.000	0.000	0.000	0.000	0.000	0.000	0.000	0.000	0.000
a9	-0.022	0.006	-0.069	-0.109	0.344	-0.265	1.751	-0.955	-1.030	0.320
b1	-0.801	-0.410	-1.217	-0.703	-0.082	-0.626	-6.046	-1.362	1.406	0.972
b2	0.711	0.196	1.569	0.756	-0.023	0.609	8.872	1.643	-1.746	-1.297
b3	0.081	0.038	0.142	0.080	0.078	0.077	0.498	0.129	-0.032	-0.025
b4	0.000	0.000	0.000	0.000	0.000	0.000	0.000	0.000	0.000	0.000
b5	-0.107	-0.033	-0.247	-0.123	-0.128	-0.113	-0.914	-0.184	0.018	0.045

The errors in fitting the thicknesses are shown in figure 14. The error in fitting is estimated by obtaining the difference between the known thickness and the thickness measured from the dual-energy decomposition equation.

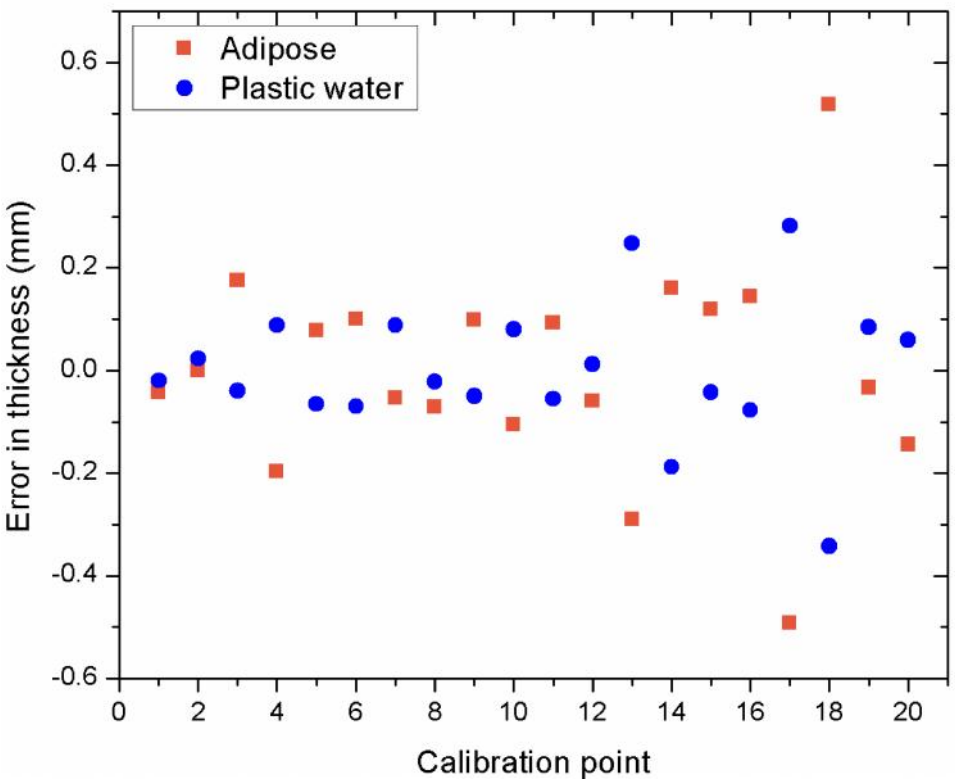

Figure 14: Fitting errors in thickness of adipose and plastic water at 29kVp

For the 20 calibration points at 29kVp, an RMS error of 0.2mm for adipose and 0.13mm for plastic water was observed.

The fitting errors in density for the 20 calibration points at 29kVp are shown in figure 15. The RMS error in density was observed to be 0.31%, shown in figure 16. Similarly, the RMS error in thickness and density was measured at the other tube voltages and the results are shown in table 5.

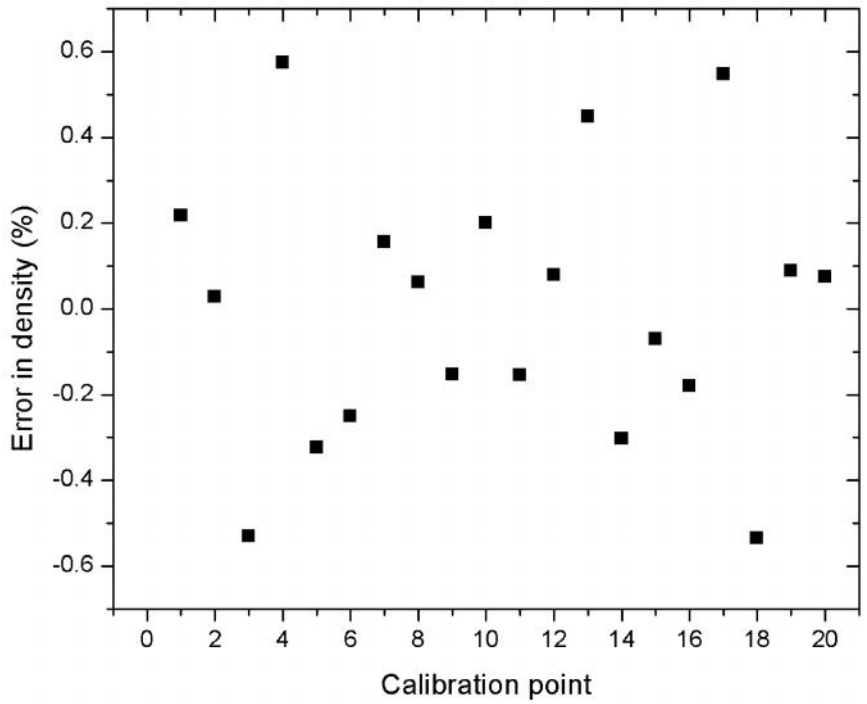

Figure 15: Fitting error in density at 29kVp

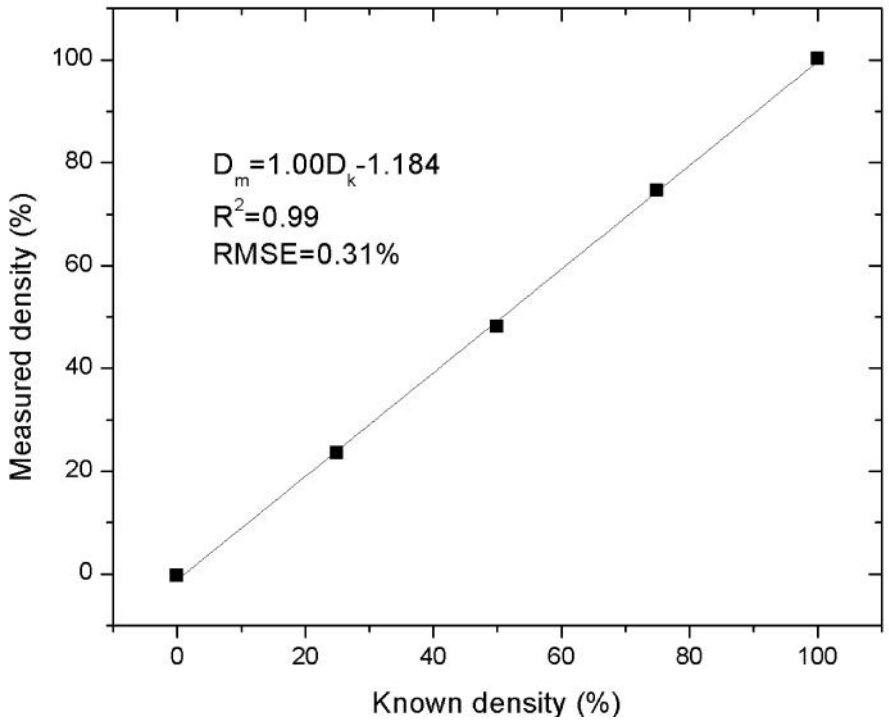

Figure 16: Plot of known versus measured density over different thickness

Table 5: RMS error in thickness and density at all tube voltages

Tube voltage	RMS error in thickness (mm)		RMS error in density (%)
	Adipose	Plastic water	
26	0.22	0.113	0.39
29	0.2	0.133	0.31
32	0.336	0.246	0.64
35	0.252	0.201	0.41
38	0.249	0.2	0.35

4.7. Discussion

The RMS error in dual energy calibration thickness estimation was found to be less than 1 mm for plastic water and adipose materials. The errors in density were observed to be less than 1% for all calibration points. The known (D_k) and measured (D_m) densities were linearly represented by $D_m=1.00D_k-1.184$ ($R^2=0.99$).

The small errors were indicative of a good match between the non-linear fitting function for dual-energy calibration and the acquired data. This establishes the effectiveness of applying the non-linear 3rd-order function in dual-energy material decomposition.

CHAPTER 5

Dual-energy based spectral mammography for characterization of breast tissue composition

Abstract

Purpose: To perform feasibility analysis of spectral mammography for breast tissue characterization in terms of water and lipid through postmortem studies

Methods: Six postmortem breasts were imaged with a photon-counting spectral mammography system. Low- and high-energy images were acquired simultaneously within a single exposure. The low- and high-energy images were decomposed to equivalent water and lipid thickness images where each pixel measurement corresponded to the thickness of water and lipid in the breast tissue above it.

The postmortem breasts were then subjected to chemical analysis to decompose them into water, lipid and protein. The result from chemical analysis was considered to be the reference standard and was compared to the quantitative data obtained from the images. Correlation between water densities measured from mammographic images and those from chemical analysis were analyzed using linear regression.

Results: Postmortem studies showed good linear correlation between the decomposed water thickness using spectral mammography and the reference standard.

Conclusion: The results demonstrate the feasibility of using spectral mammography to represent the breast tissue composition, in terms of water and lipid accurately. This quantitative information can be used as an indicator of breast cancer risk.

5.1. Introduction

Breast cancer is one of the most frequently diagnosed cancers amongst American Women. Currently, mammography is the standard imaging modality used in breast cancer screening. Despite its impressive advantages in detection performance, imaging time, and cost-effectiveness, its limitations is widely recognized [23-26]. The most critical for early detection in breast cancer screening is to increase the specificity of tumor detection and reduce the overall population dose by eliminating screening examinations to avoid recalling healthy women for unnecessary needle biopsy and radiation exposure.

Previous reports, addressing diffuse optical spectroscopy have suggested that malignant tumors have reduced lipid (∼20%) and increased water (>50%) contents compared to normal breast tissue [27-30]. In addition, other reports suggest a positive correlation between increased tissue water content and carcinogenesis [31]. It has been suggested that increased cell water content not only promotes cell division and oncogene expression, but also accelerates cells' respiration rate, which enhances their ability to compete for nutrients with normal cells, [32] and that the degree of malignancy increases with the degree of cell hydration [33]. These reports indicate that mammography's sensitivity and specificity may be improved if breast tissue composition can be accurately measured, in order to better characterize lesions according to their composition.

A previous report has proposed to characterize breast tissue using a three-material compositional measure of water, lipid, and protein contents using dual-energy mammography [34]. Dual-energy mammography is based on the principle that different breast tissues have different effective atomic numbers (Z) that can provide individual quantitative thickness measurements for each tissue.

However, three-material decomposition using dual-energy mammography requires accurate breast thickness measurement as the third independent physical measurement. The fundamental limitation is that the X-ray attenuation properties of water, lipid, and protein have small differences in their diagnostic energy range [34]. Therefore, three-material decomposition will require very accurate breast thickness measurement, which is not feasible. This project, however, presents a two-material decomposition model to characterize the chemical composition of breast tissue using dual-energy spectral mammography.

Previous reports presented techniques that use the standard screening mammogram as the low- energy image and an additional exposure at a higher kVp [35, 36]. The need to acquire the additional high-energy image slightly increases the mean glandular dose along with the possibility of introducing misregistration artifacts due to patient motion between the two image acquisitions.

Energy sensitive, photon-counting X-ray detectors that sort the detected photons according to their energies are employed to measure breast tissue composition. Recently, a photon-counting spectral mammography system based on scanning multi-slit Si-strip detectors has been reported [37-41]. A previous study has reported that this system is capable of breast tissue thickness quantification without any additional exposures [36]. Dual-energy data can be

acquired with a single exposure and the energy-resolving capability prevents spectral overlap in dual-energy decomposition. It also eliminates misregistration due to motion artifacts between the two exposures in dual kVp technique. Additionally, the electronic readout noise can be effectively eliminated by proper selection of background threshold which can further improve detection efficiency. A previous report shows six-fold increase in detectability for dense breast with high anatomical noise [40]. In addition, the scanning multi-slit geometry helps eliminate scattered radiation, which remains a major limitation for charge-integrating flat panel detectors used form mammography.

5.2. Theory

This technique is based on the principle that different tissues have different atomic numbers thereby, having different X-ray attenuation coefficients. X-ray attenuation is mainly due to Compton scatter and photoelectric absorption. Dual energy imaging makes use of the energy dependence of the attenuation coefficients of materials. In the mammographic energy range, a linear combination of any two materials having different and low atomic numbers can approximately simulate the energy-dependent attenuation of a third material of a given thickness

$$t_{sample} \times \mu_{sample}(E) = t_1 \times \mu_1(E) + t_2 \times \mu_2(E)$$

The two constituent materials form the basis materials and the associated normalized thicknesses $\frac{[t_1, t_2]}{t_{sample}}$ are unique descriptors of the energy-dependent sample attenuation μ_{sample} given the known attenuations of the basis materials μ_1 and μ_2. For a known total sample thickness t_{sample}, the thickness of the two constituent materials can be estimated by the measurement of attenuation at two different energies. This would produce a non-linear system of two equations which is sufficient to arrive at the constituent material thicknesses t_1 and t_2.

The main components of breast tissue are water, lipid and protein. Our previous analysis of postmortem breasts showed that the average water, lipid and protein contents were 34.2%, 59.9%, and 5.8%, respectively; therefore, it is possible to characterize breast tissue in terms of water and lipid, given the small contribution of protein to the total mass.

It has also been established that malignant tissue contains higher quantities of water and lower quantities of lipid than normal tissue. Thus, it is essential to decompose the sample tissue in terms of water and lipid as the two basis materials in dual energy breast material decomposition.

In the obtained dual energy images, each pixel's low- and high-energy signals (S_L and S_H) can be written as functions of the water and lipid content thicknesses (t_W and t_l)

$$\begin{pmatrix} \mu_w^L & \mu_l^L \\ \mu_w^H & \mu_l^H \end{pmatrix} \begin{pmatrix} t_w \\ t_l \end{pmatrix} = \begin{pmatrix} S_L \\ S_H \end{pmatrix}$$

Where μ_W^L, μ_l^H, $\mu_W^H$and $\mu_l^L$are the linear attenuation coefficients of water and lipid at low (*L*) and high (*H*) energy bins, respectively. The thickness of water and lipid in the region above each pixel can then be derived by linear numerical matrix inversion, and each pixel's proportions of water and lipid in the breast can be determined.

For the purpose of calibration, a non-linear least-squares fitting function is applied, which employs the log signals and known thicknesses of lipid or water to estimate the corresponding coefficients.

$$t_i = \frac{a_0 + a_1 S_L + a_2 S_H + a_3 S_L^2 + a_4 S_L S_H + a_5 S_H^2 + a_6 S_L^3 + a_9 S_H^3}{1 + b_1 S_L + b_2 S_H + b_3 S_L^2 + b_4 S_L S_H + b_5 S_H^2}$$

If a water thickness image is considered, the pixel value reads the integrated thickness of water in the column of tissue above that particular pixel. If this region includes the lesion, the decomposed water thickness would be a sum of the lesion water thickness and that of the normal tissue above and below the lesion. The water content of the lesion can be estimated by subtracting the total decomposed water signal from a region outside of the lesion assuming uniform water content distribution over the entire region. These subtracted signals can thus help characterize lesions based on the lipid and water contents.

5.3. Materials and Methods

5.3.1. Calibration procedure

For the convenience of clinical implementation, dual-energy calibration was performed initially using plastic water and adipose-equivalent plastic phantoms as basis materials. But the X-ray attenuation property of the adipose phantom is different from lipid present in breast tissue mainly due to the presence of water in adipose tissue. Thus two techniques were used to convert the dual-energy decomposition measurements from plastic phantom thicknesses into true water and lipid basis. The first method employed theoretical x-ray attenuation coefficients of water and lipid in the mammographic energy range. Least-square fitting was applied to obtain the conversion matrix. The second method was based on experimental calibrations. Low-and high-energy signals of pure water and lipid of known thicknesses were measured. A non-linear rational function was applied to correlate the decomposed thicknesses to the known values in order to determine the conversion coefficients. Breast tissue of a given thickness ($\mu_B t_B$) can be decomposed into two sets of basis materials: (1) plastic water (μ_{pw}) and adipose phantom (μ_{ap}); and (2) water (μ_w) and lipid (μ_l). In a matrix notation, this is written as:

$$\mu_B t_B = T_p \mu_p = T_{wl} \mu_{wl}, \text{ where}$$

$$T_p = [t_{pw} \quad t_{ap}], \mu_p = \begin{bmatrix} \mu_{pw} \\ \mu_{ap} \end{bmatrix}, T_{wl} = [t_w \quad t_l], \mu_{wl} = \begin{bmatrix} \mu_w \\ \mu_l \end{bmatrix}.$$

In addition, the matrices μ_p and μ_{wl} are related through a conversion matrix A_{wl}, which contains the equivalent thicknesses of water and lipid for the CIRS tissue-equivalent calibration phantoms:

$$A_{wl} = \begin{bmatrix} a_{pw}^w & a_{pw}^l \\ a_{ap}^w & a_{ap}^l \end{bmatrix}$$

A_{wl} was determined through simulations and also through experimental calibrations. Thus the relationship between the true water and lipid contents in the breast and the measured data from phantom calibration becomes

$$T_p\mu_p = T_{wl}\mu_{wl} = T_{wl}A_{wl}\mu_p \Rightarrow T_{wl} = T_pA_{wl}^{-1}$$

Theoretical method

This method involved using the theoretical attenuation coefficients of the basis materials shown in table 6 with the equations presented above and the known thickness and attenuation of plastic water and adipose-equivalent plastic.

Experimental method

Experimental calibrations were performed using liquid water and lipid samples of well-controlled thicknesses.

For this purpose, different thicknesses of liquid water and lipid extracted from postmortem breast were individually imaged using the spectral mammography system (MicroDose SI, Philips) at different tube voltages (26, 29, 32, 35 and 38kVp). The thicknesses ranged from 0 to 8cm in steps of 0.5cm (table 7). The conversion factors were calculated from the above mentioned equations.

Table 6: Mass attenuation coefficient of water and lipid in the mammographic energy range

Energy (kVp)	Mass attenuation coefficient	
	Water	Lipid
20	0.80767	0.47830
21	0.73127	0.44356
22	0.65486	0.40892
23	0.60436	0.38588
24	0.55386	0.36285
25	0.50877	0.34248
26	0.47656	0.32800
27	0.44435	0.31352
28	0.41725	0.30067
29	0.39601	0.29150
30	0.37530	0.28239
31	0.35896	0.27382
32	0.34265	0.26596
33	0.33080	0.26008
34	0.31895	0.25421
35	0.30709	0.24833
36	0.29894	0.24403
37	0.29079	0.23973
38	0.28263	0.23583
39	0.27478	0.23224
40	0.26800	0.22880

For the purpose of calibration, after applying the theoretical and experimental methods in determining the conversion factors, non-linear least-squares fitting function was applied to the

Table 7: Known density and thickness of water and lipid at different calibration points

Calibration point	Known density (%)	Known lipid thickness (cm)	Known water thickness (cm)
1	100.00	0.00	1.98
2	78.35	0.43	1.55
3	56.33	0.86	1.11
4	34.35	1.30	0.68
5	14.63	1.71	0.29
6	100.00	0.00	4.01
7	78.40	0.86	3.12
8	57.02	1.72	2.28
9	35.44	2.58	1.41
10	14.64	3.41	0.58
11	100.00	0.00	6.02
12	78.60	1.29	4.74
13	57.18	2.56	3.42
14	35.66	3.84	2.13
15	14.65	5.11	0.88
16	100.00	0.00	8.01
17	78.54	1.73	6.32
18	57.31	3.41	4.58
19	35.78	5.12	2.85
20	14.66	6.82	1.17

log signals and known thicknesses of lipid and water to estimate the corresponding fitting coefficients.

$$t_i = \frac{a_0 + a_1 S_L + a_2 S_H + a_3 S_L^2 + a_4 S_L S_H + a_5 S_H^2 + a_6 S_L^3 + a_9 S_H^3}{1 + b_1 S_L + b_2 S_H + b_3 S_L^2 + b_4 S_L S_H + b_5 S_H^2}$$

5.4. Postmortem study

The main motivation of a postmortem study was to evaluate the accuracy of the proposed decomposition technique.

5.4.1. Sample preparation

This technique was experimentally validated through a postmortem breast study. Three pairs of postmortem breasts (n=6) were obtained from the university willed body program. The pectoralis muscle was removed and the samples were wrapped with clear wrap to prevent the loss of water.

5.4.2. Image acquisition and processing

The postmortem breasts were imaged using a dual-energy mammography system (MicroDose SI, Philips). The samples were imaged at different tube voltages (26-35kVp) and currents (10-14.5mAs) based on compressed breast thickness. High- and sum- energy images were acquired for each breast. Low-energy images were obtained by the subtraction of high-energy images from the corresponding sum-energy images. All image processing steps were carried out using ImageJ. Log-signal images (μt) for low- and high- energy images (I) were obtained by the application of Beer-Lambert equation using the corresponding energy open-field images (I_o).

$$\mu t = -log\left({}^{I}/_{Io}\right)$$

The low- and high- energy attenuation coefficient images were decomposed into water and lipid thickness images using previously determined calibration coefficients. ROIs were drawn to encompass the entire breast and the thickness of the basis material in the whole breast was measured, shown in figure 17. The density of water and lipid and the volumetric composition of the two materials in the samples were calculated. Total breast volume was calculated by summing the product of the area per pixel by the combined thickness of water and lipid for all

points in the ROI. The thickness images were represented with color maps to better represent the water and lipid quantities in the breasts as shown in figure 18.

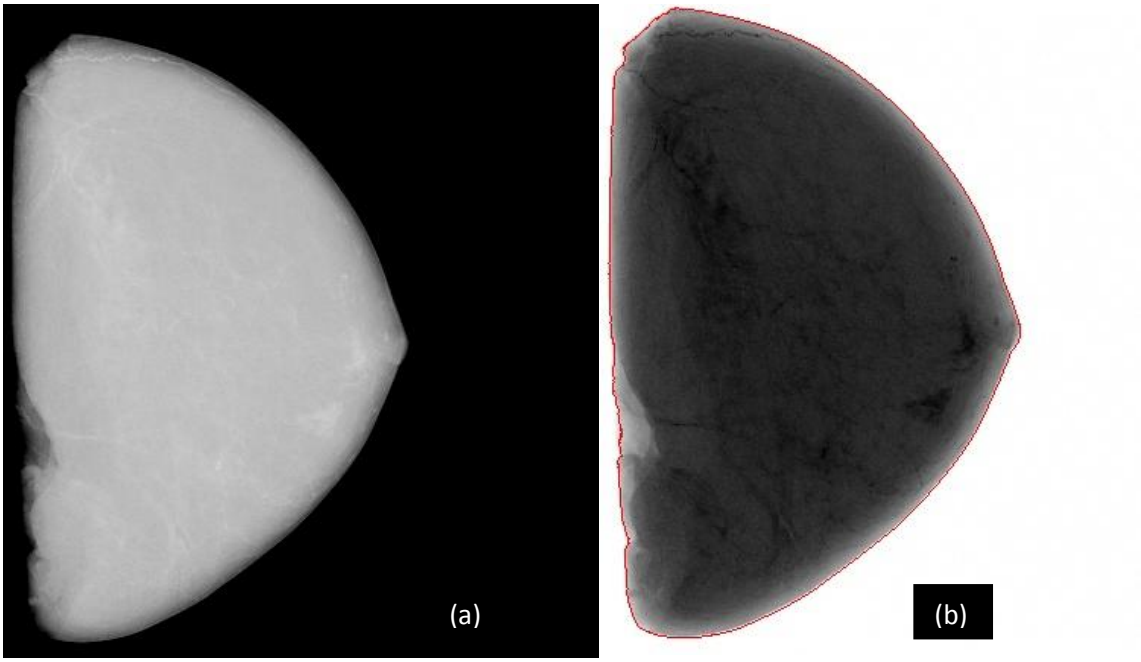

Figure 17: (a) Mammographic image of left postmortem breast (b) Water thickness image of the breast with ROI (red) surrounding the entire breast volume

5.4.3. Chemical analysis

Chemical analysis is a standard procedure developed by the United States Department of Agriculture and is employed to measure the contents of water, lipid and protein in a given sample.

Whole volumes of the postmortem breasts were chemically decomposed immediately after imaging [42]. The samples were cut into small pieces and put in aluminum baking trays. The trays were placed in a vacuum oven maintained at 95^{o}C for about 48hours until all the water

evaporated. The baking time and oven temperature depended on the sample sizes. The samples were taken out of the oven and weighed. The difference in pre- and post- bake weights were attributed to water content in the samples. The dried samples were then mixed with petroleum ether and ground into slurry to dissolve the lipid content from the tissue into the ether. This solution was then vacuum filtered through a pre-weighed Buchner funnel. Additional petroleum ether was used to wash the sample to remove any residual lipid content. The sample tray was re-weighed and the dry sample retained in it was assumed to be protein. The difference in mass was assumed to be lipid. The ether solution now contained lipid, which was then isolated from the solution by evaporating

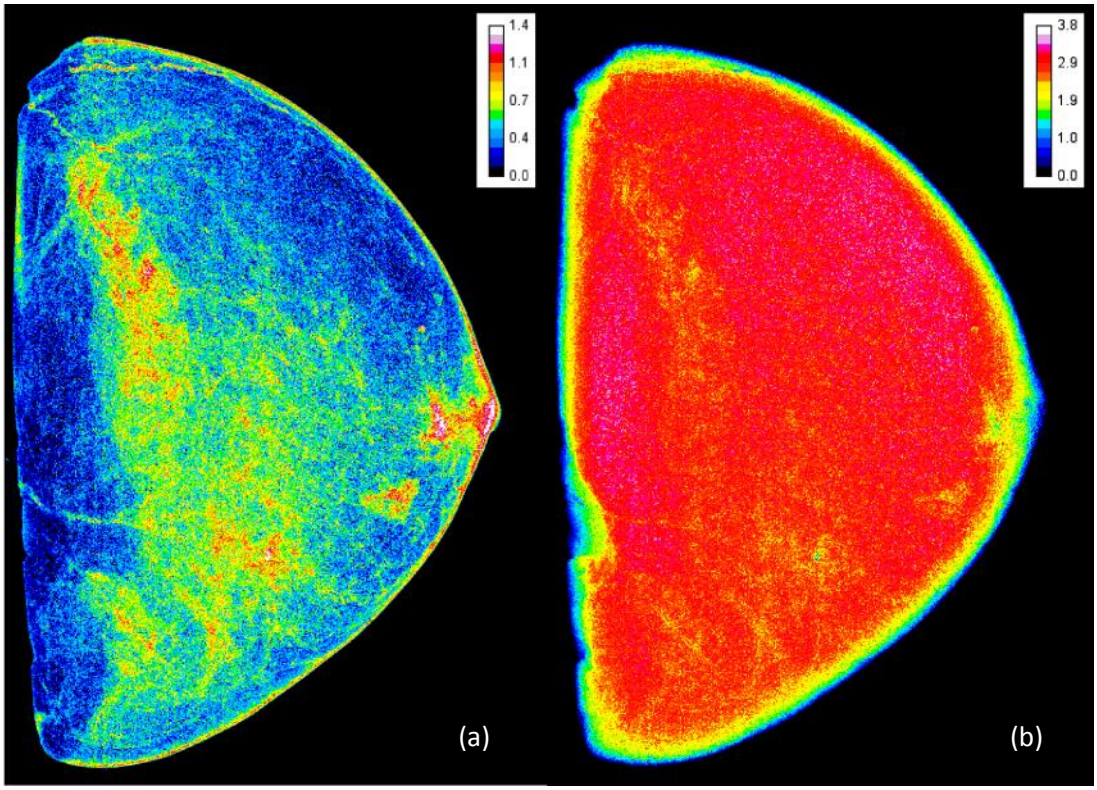

Figure 18: (a) Water thickness image (b) Lipid thickness image of the breast in figure 17

the petroleum ether by heating under vacuum distillation. The mass of protein and isolated lipid content were each weighed, with the balance assumed to be water. The volumetric percentages of water, lipid and protein content were calculated and compared to the results obtained from the images.

5.5. Quantities compared

Water and lipid content (Q_w and Q_l) were determined from the dual-energy images and chemical analysis. The quantity of protein Q_p was also obtained from chemical analysis. Volumetric percentages of water and lipid obtained from the images, was compared to that obtained from chemical analysis. The measured densities from the two methods were also evaluated.

$$Density = \left(\frac{M_w/1}{M_w/1+M_l/0.92+M_p/1.35}\right) 100$$

5.5. Error analysis

The RMS error (RMSE) in measured density was calculated using the following equation:

$$RMSE = \frac{1}{\sqrt{n}} \sqrt{\sum_{i=1}^{n} (D_m - D_k)^2}$$

5.6. Results

5.6.1. Calibration

The fitting coefficients for water and lipid at different tube voltages are shown in table 8.

The errors in fitting the thicknesses of water and lipid are shown in figure 19. The error in fitting is estimated by obtaining the difference between the known thickness and the thickness measured from the dual-energy decomposition equation.

Table 8: Fitting coefficients for water and lipid at different tube voltages

Coefficient Index	26kVp		29kVp		32kVp		35kVp		38kVp	
	Lipid	Water	Lipid	Water	Lipid	Water	Lipid	Water	Lipid	Water
a0	-0.92	0.52	-0.93	0.62	-2.18	1.14	-3.13	1.89	-1.53	0.59
a1	-17.02	10.18	-17.02	10.29	-22.77	11.46	-22.77	12.99	-25.11	13.28
a2	25.73	-14.05	24.09	-13.42	32.74	-14.94	29.59	-17.15	30.36	-13.44
a3	0.68	-0.41	-1.01	-0.30	-20.30	-1.07	37.36	-4.20	-33.11	9.87
a4	-0.46	0.07	0.15	-0.05	60.87	0.01	-104.99	5.96	89.01	-24.72
a5	-1.77	0.89	2.36	0.32	-45.03	1.53	76.47	-0.79	-56.23	13.39
a6	0.06	-0.02	-0.06	0.07	-0.19	0.12	-0.65	0.29	0.11	0.07
a7	0.00	0.00	0.00	0.00	0.00	0.00	0.00	0.00	0.00	0.00
a8	0.00	0.00	0.00	0.00	0.00	0.00	0.00	0.00	0.00	0.00
a9	-0.02	0.02	-0.06	-0.09	0.37	-0.20	1.30	-0.62	-0.86	0.16
b1	-0.81	-0.37	-1.24	-0.53	0.35	-0.55	-3.99	-0.66	1.41	0.55
b2	0.72	0.15	1.60	0.49	-0.66	0.48	5.84	0.61	-1.76	-0.68
b3	0.08	0.04	0.14	0.06	0.05	0.07	0.36	0.08	-0.03	0.00
b4	0.00	0.00	0.00	0.00	0.00	0.00	0.00	0.00	0.00	0.00
b5	-0.11	-0.03	-0.25	-0.09	-0.07	-0.09	-0.65	-0.09	0.02	0.01

For the 20 calibration points at 29kVp, an RMS error of 0.17mm for lipid and 0.105mm for water was observed.

Table 9: RMS errors in thickness and density of water and lipid at different tube voltages

Tube voltage (kVp)	RMS error in thickness (mm)		RMS error in density (%)
	Lipid	Water	
26	0.199	0.106	0.35
29	0.17	0.105	0.26
32	0.285	0.198	0.54
35	0.214	0.167	0.34
38	0.211	0.165	0.3

The fitting errors in density for the 20 calibration points at 29kVp are shown in figure 20. The RMS error in density was observed to be 0.26%. Similarly, the RMS error in thickness and density was measured at the other tube voltages and the results are shown in table 9.

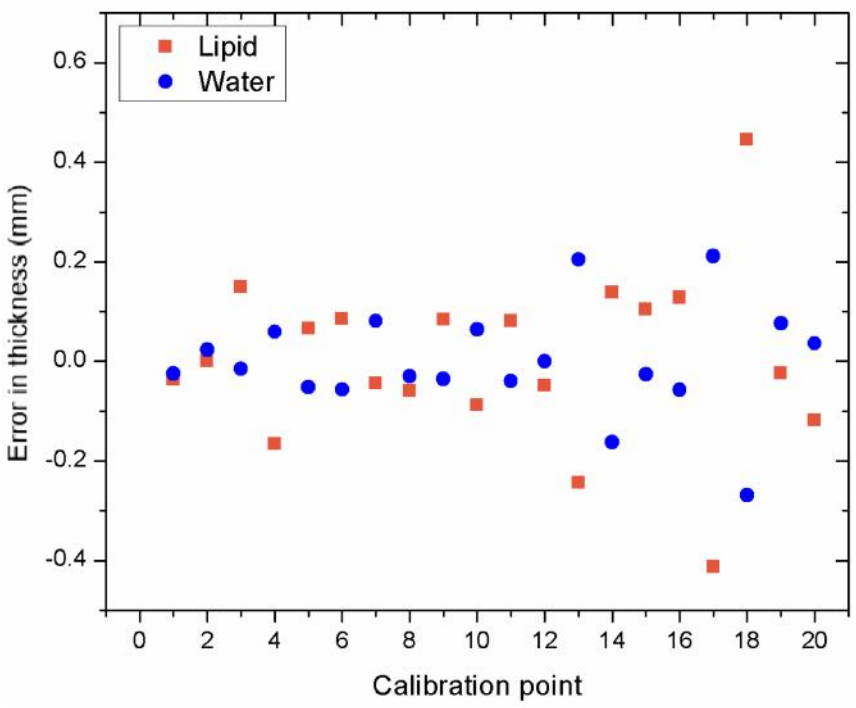

Figure 19: fitting error in thickness of lipid and water for all calibration points

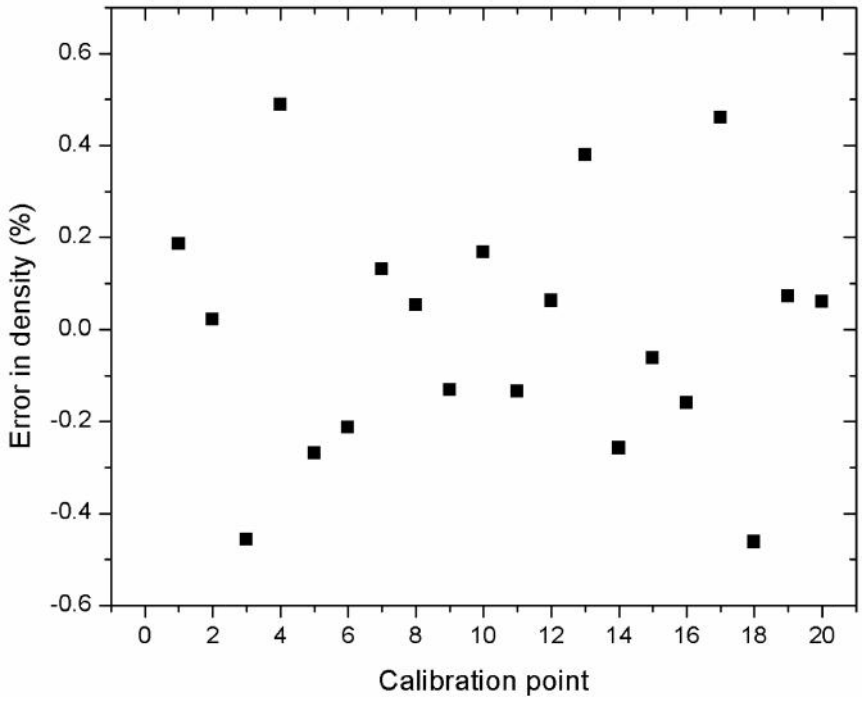

Figure 20: Fitting error in density for all 20 calibration points

5.6.2. Postmortem study

Figure 21 shows the volumetric percentages of water and lipid as measured by the dual-energy decomposition of images and the reference gold standard chemical analysis for one of the postmortem breasts. Comparison of the measured quantities revealed a standard deviation of 0.4% for water and 2.78% for lipid. Figure 22 shows volumetric percentage of water measured from chemical analysis and dual-energy decomposition plotted against each other for different breast samples. A linear relationship is observed between the two datasets that can represented by $V_d=1.21V_c-3.60$ ($R^2=0.95$).

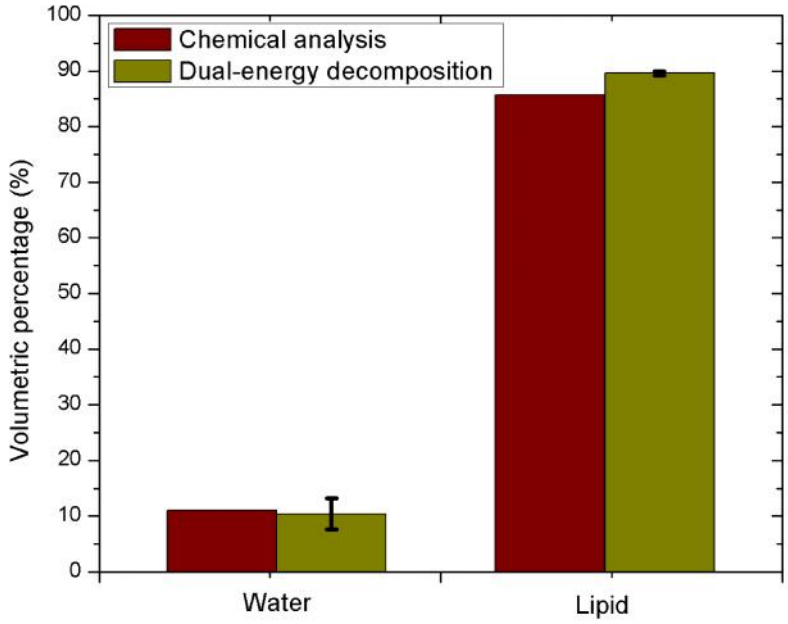

Figure 21: Comparison of volumetric percentages of water and lipid as measured by chemical analysis and dual-energy images for a breast sample

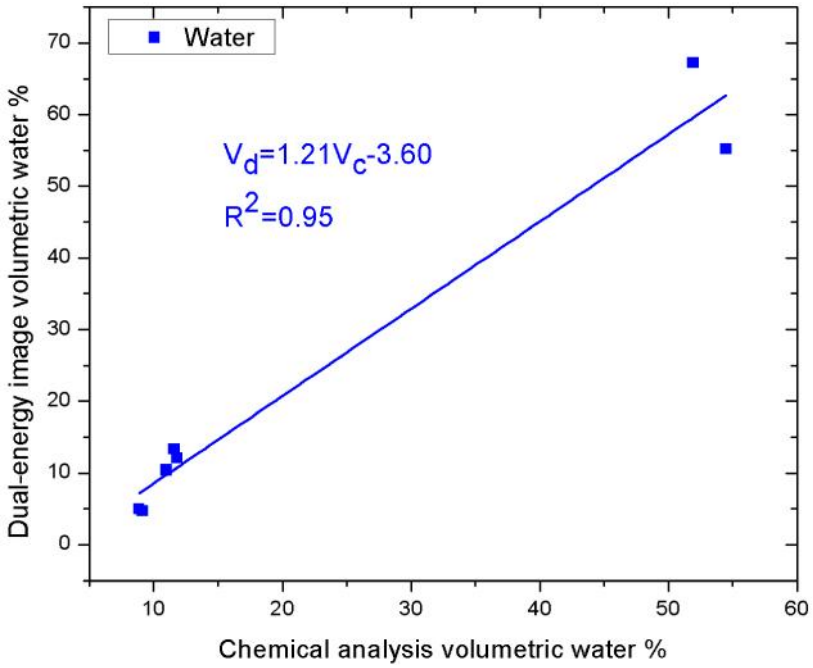

Figure 22: Comparison of volumetric water percentage measured by chemical analysis and dual-energy images for 6 postmortem breasts

Figure 23 shows volumetric percentage of lipid measured from chemical analysis and dual-energy decomposition plotted against each other for different breast samples. A linear relationship is observed between the two datasets that can represented by V_d=1.03V_c+1.11 (R^2=0.95).

Discussion

The RMS error in dual energy calibration thickness estimation was found to be less than 1 mm for both water and lipid. The errors in density were observed to be less than 1% for all calibration points at all tube voltages.

The small errors were indicative of a good match between the non-linear fitting function for dual-energy calibration and the acquired data. This establishes the effectiveness of applying the non-linear 3rd-order function in dual-energy material decomposition.

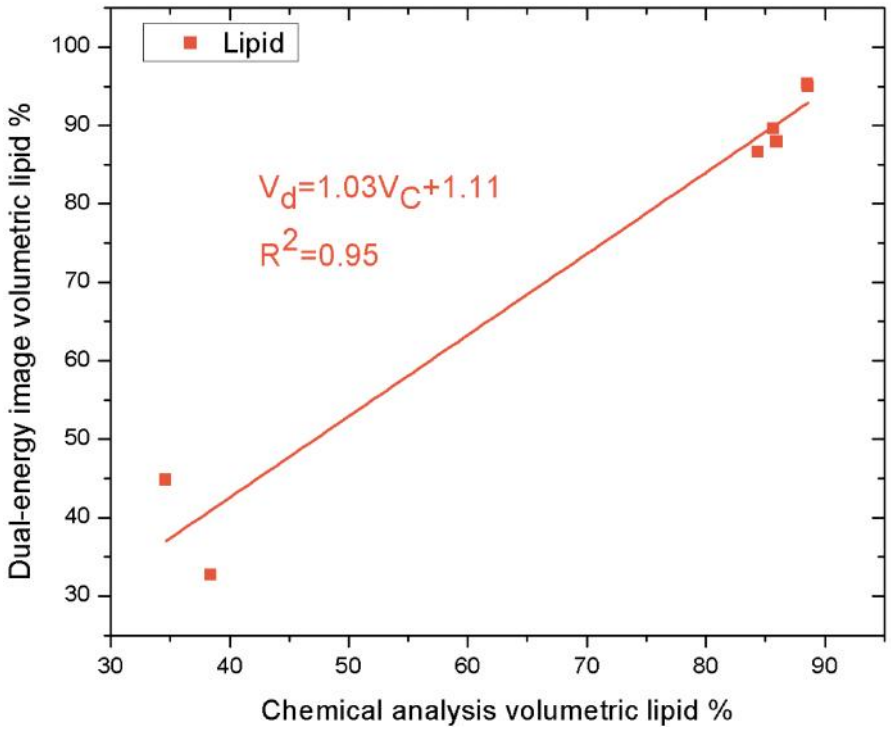

Figure 23: Comparison of volumetric lipid percentage measured by chemical analysis and dual-energy images for 6 postmortem breasts

Results from Figure 22 and 23 also show a linear relationship between V_d and V_c for volumetric percentage measurements of water and lipid respectively. An offset and non-unity slope in the linear relationship between the volumetric percentage of water and lipid as measured from dual-energy images and chemical analysis may be due to a significant amount of water being present in the adipose tissue. Another possibility for error or offset may be due to the fact that

in the dual-energy images, protein in the tissue is also represented in terms of water and lipid unlike in case of chemical analysis where protein is extracted as a third component. This resulted in further computation to represent protein mass (P) obtained from chemical analysis in terms of water (W_p) and lipid (L_p).

In the dual-energy images the quantity of water measured *(W^1)* is the sum of water from protein and actual water itself. Similarly the quantity of lipid measured *(L^1)* is the sum of lipid from protein and actual lipid.

$$W^1 = W + W_p$$

$$L^1 = L + L_p$$

The attenuation due to protein (μ_p) can be represented as a linear combination of attenuation by water (μ_w) and lipid (μ_l) with the coefficients a_1 and a_2 respectively.

$$\mu_p = a_1\mu_w + a_2\mu_l$$

The coefficients were estimated by using the known attenuation coefficients of protein, water and lipid in the mammographic energy range (10-40 keV)

The coefficients were found to be:

$a_{1=}$ 0.46807 and $a_{2=}$ 0.50532

The contribution of protein to water and lipid can be represented by the following equations using the protein mass (P) estimated from chemical analysis of the breast sample:

$$W_p = a_1 P$$

$$L_p = a_2 P$$

The water and lipid contributed by protein was then added to the actual water and lipid content measured. It was observed that the change in volumetric percentage of water and lipid was small ~0.02%. The samples under consideration contained a volumetric percentage of 2-10% protein thus, not contributing largely to volumetric changes in water and lipid. It can be concluded that the error may be due to water present in the adipose tissue.

This experiment ultimately helps determine the usefulness of dual energy mammography in quantifying the chemical composition for samples of unknown composition when a two compartment model of water and lipid is assumed.

CHAPTER 6

Dual-energy based spectral mammography for characterization of breast lesion composition: A postmortem study

Abstract

Purpose: To investigate whether suspicious breast lesions can be characterized by decomposition into constituent materials using dual-energy spectral mammography.

Methods: Postmortem breasts were imaged in the mammographic energy range 26-35kVp using a silicon based spectral mammography system. Plastic water and adipose-equivalent lesion disks (0.5cm in thickness and 2cm in diameter) of varying densities (0-100% plastic water) were inserted into the breast tissue during imaging. Dual-energy decomposition of breast images was performed based on calibration coefficients obtained from a previous phantom study. The low- and high- energy breast images were decomposed into constituent water and adipose-equivalent thickness images with each pixel value indicating the actual thickness of the constituent basis material. The thickness of water and adipose in the lesion disks were then calculated by choosing circular, concentric ROIs within and around the disks. The resulting water densities in the lesion disks were estimated and compared with the known densities of the disks.

Results: The measured (D_m) and known (D_k) water density measurements of the lesions were related as $D_m = 1.08D_k + 0.84$ (R^2=0.99). A root-mean-square (RMS) error of 9.24% was calculated.

Conclusion: The results indicated that dual-energy spectral mammography can be used to quantify the composition of breast lesions, which may improve the predictive power for malignant lesions in screening mammography.

6.1. Introduction

The most critical for early detection in breast cancer screening is to increase the specificity of tumor detection to avoid recalling healthy women for unnecessary needle biopsy and radiation exposure.

Previous reports have suggested that malignant tumors have reduced lipid (~20%) and increased water (>50%) contents compared to normal breast tissue [27-30]. In addition, other reports suggest a positive correlation between increased tissue water content and carcinogenesis [31]. It has been suggested that the degree of malignancy increases with the degree of cell hydration [33]. These reports indicate that mammographic tumor specificity may be improved through quantification of breast lesion composition.

This project proposes to characterize breast lesions according to their chemical composition, in terms of water and lipid contents, with a low-dose photon-counting spectral mammography system based on multi-slit Si-strip detectors. The proposed technique is expected to improve the positive predictive values and reduce the number of false-positive results without additional radiation dose.

The accuracy in lesion characterization also depends on the proper choice of the calibration material. The traditional two-compartment model generally decomposes breast tissue into fibroglandular and adipose tissues. However, the two-compartment model has not been used

to detect high density masses in breast tissue, because it cannot fully eliminate any of the three major components which are water, lipid and protein. Moreover, the current two-compartment model suffers large uncertainty from system calibration due to the wide variations in the chemical composition of the fibroglandular and adipose tissue [43, 44]. Extending the traditional model into a water-lipid system not only enables lesions to be characterized according to their actual chemical composition, but also standardizes calibration phantom used in dual-energy decomposition. However, both water and lipid are liquid, which makes them difficult to handle in a clinical environment. Therefore, solid plastic calibration phantoms, which have similar X-ray attenuation properties as water and adipose were employed. Plastic Water and adipose-equivalent phantoms (CIRS, Norfolk, VA) were used for this purpose.

6.2. Materials and Methods

6.2.1. Sample preparation

Four pairs of postmortem breast samples (n=8) were obtained from the willed body program. The pectoral muscles from the samples were removed and the samples were wrapped using clear plastic wrap to prevent the loss of water during imaging.

6.2.2. Image acquisition and processing

The current study was conducted with postmortem breasts which were imaged with a silicon photon counting mammography system (MicroDose SI, Philips). Plastic water and adipose-equivalent plastic disks (CIRS Inc., Norfolk VA) that closely resemble the attenuation coefficients of real water and adipose were embedded in the breast tissue. The disks are 0.5cm in height

and have a fixed diameter of 2cm. The table 10 shows the chemical composition of the lesion disks.

Table 10: Chemical composition of plastic water and adipose-equivalent plastic

	Mass fraction	
Elements	**CIRS Adipose**	**Plastic Water**
H	0.098	8.100E-02
C	0.714	6.720E-01
N	0.020	2.400E-02
O	0.163	1.990E-01
Cl	0.003	1.000E-02
Ca	0.001	2.300E-02

The density of plastic water and adipose vary from 0 to 100% in steps of 20%. The adipose-equivalent plastic mimics the attenuation of 15% water and 85% lipid; plastic water has attenuation similar to pure water. The samples were imaged at different tube voltages (26-35kVp) and currents (10-14.5mAs) based on compressed breast thickness. High- and sum-energy images were acquired for each breast. Low-energy images were obtained by the subtraction of high-energy images from the corresponding sum-energy images. Attenuation coefficient images (μt) for low- and high- energy images (I) were obtained by the application of Beer-Lambert equation using the corresponding energy open-field images (I_o).

$$\mu t = -log\left({}^{I}/_{Io}\right)$$

6.2.3. Image based quantification of lesion composition

The low- and high- energy attenuation coefficient images were decomposed into water and adipose-equivalent thickness images using previously determined calibration coefficients. Two circular ROIs were chosen in order to calculate the thickness of the two basis materials in the lesion disks, shown in figure24. Large donut shaped ROIs were drawn around the lesion disks to estimate thickness of the basis material in the background. Smaller ROIs were drawn within the disks to estimate the thicknesses of the basis materials in the disks and the column of tissue above and below the disks. The measurements from the two ROIs were subtracted to obtain the difference between the lesion phantom and the tissue background. Corresponding density of plastic water in the lesion disks was calculated from the ratio of water thickness (t_{pw}) to the total thickness (t_T) of the disk, where total thickness is the sum of plastic water and adipose-equivalent thicknesses in the lesion.

$$Plastic\ water\ density = t_{pw}/t_T$$

$$t_T = t_{pw} + t_{ad}$$

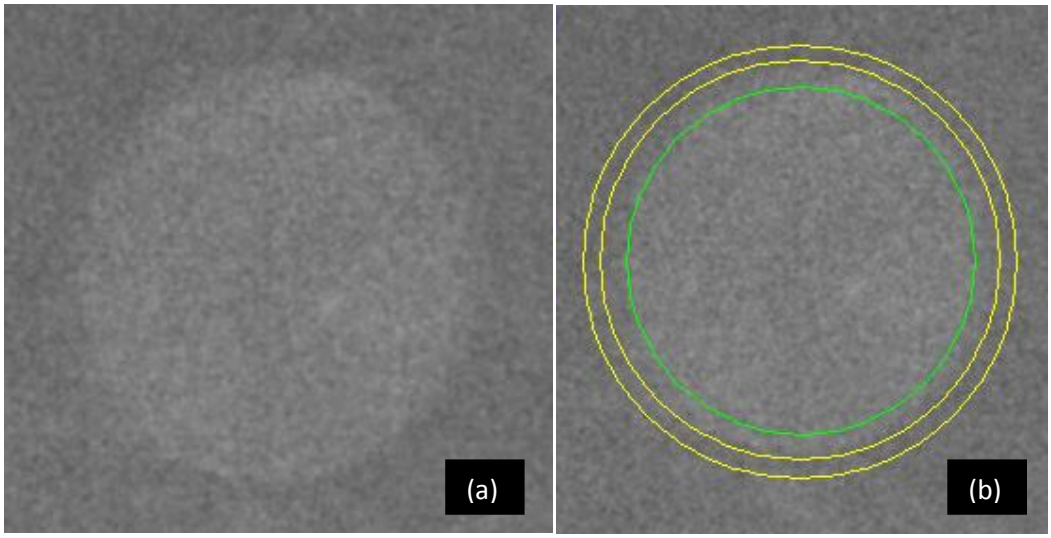

Figure24: (a) 80% plastic water lesion phantom disk (b) Lesion disk marked by larger outer donut ROI (yellow) and smaller inner ROI (green)

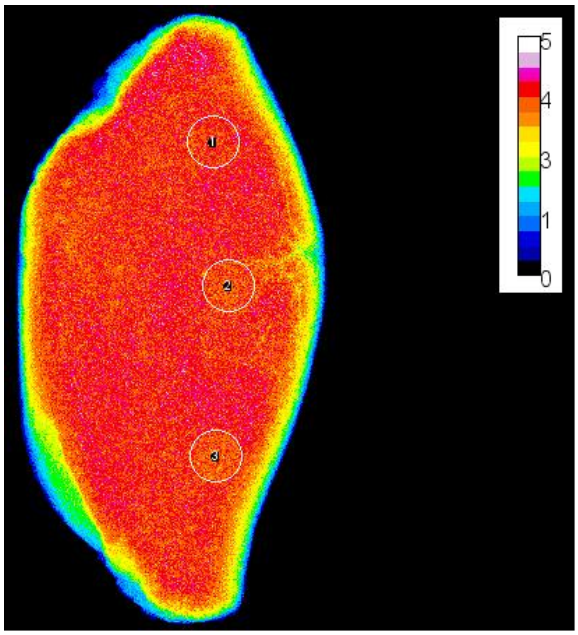

Figure 25: Color map representation of postmortem breast image with three lesion phantoms

6.2.4. Quantities compared

Measured thickness of plastic water lesions phantoms were compared to the known thicknesses. The measured and known plastic water densities were also plotted against each other.

6.3. Error analysis

The RMS error (RMSE) in measured density was calculated using the following equation:

$$RMSE = \frac{1}{\sqrt{n}} \sqrt{\sum_{i=1}^{n} (D_m - D_k)^2}$$

6.4. Results

The inserted phantom thicknesses were measured and compared to the known thicknesses. For plastic water, excellent linear relation was seen between the two and the quantities were given by the equation $T_m=0.97T_k+0.03$ ($R^2=0.99$). An RMS error of 0.26mm was calculated for plastic water thickness estimation, shown in figure 26.

In case of adipose thickness measurement, very good linear relation was observed between the known and measured thicknesses as shown in figure 27. The relation could be represented by $T_m=0.97T_k-4.82$ ($R^2=0.96$). An RMS error of 0.21mm was estimated.

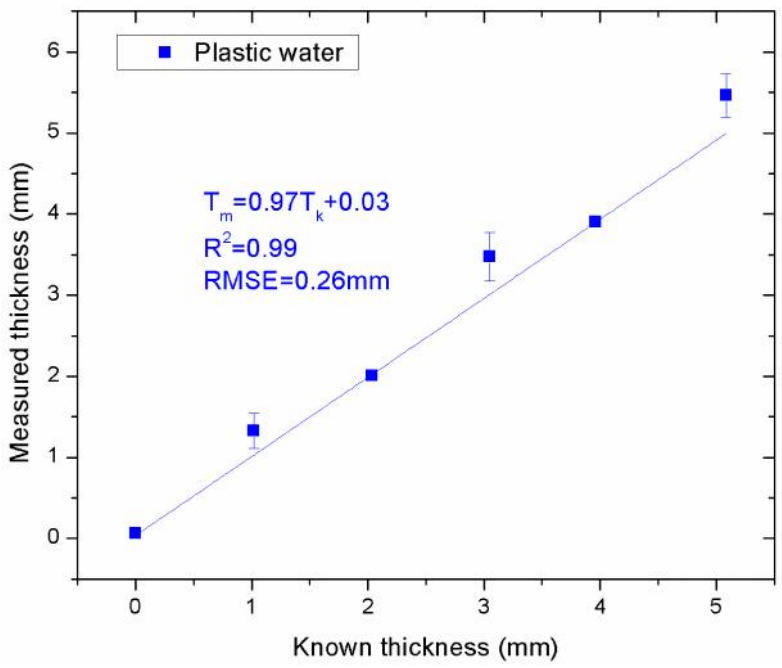

Figure 26: Comparing known and measured plastic water thicknesses in the lesions

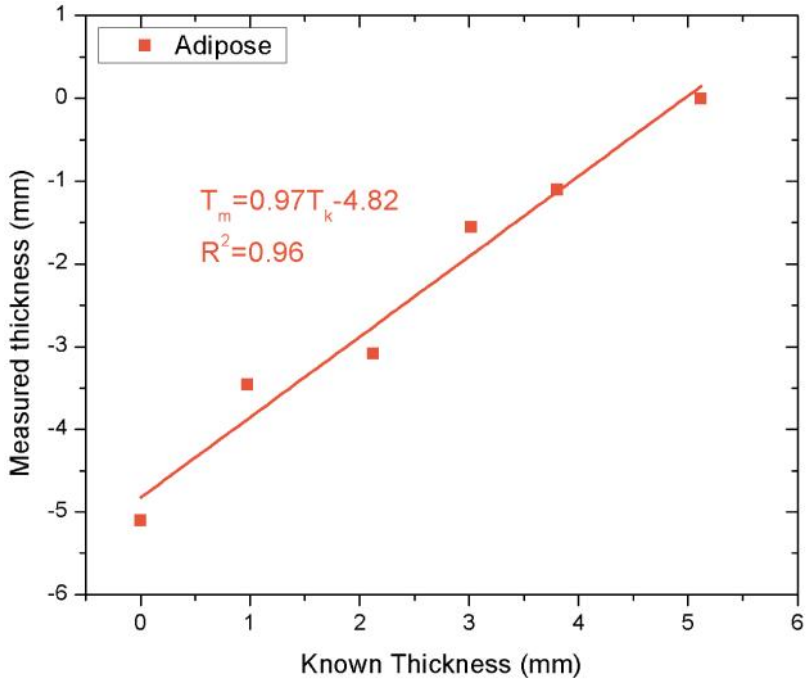

Figure 27: Plot of known and measured adipose thickness in the inserted lesion phantoms

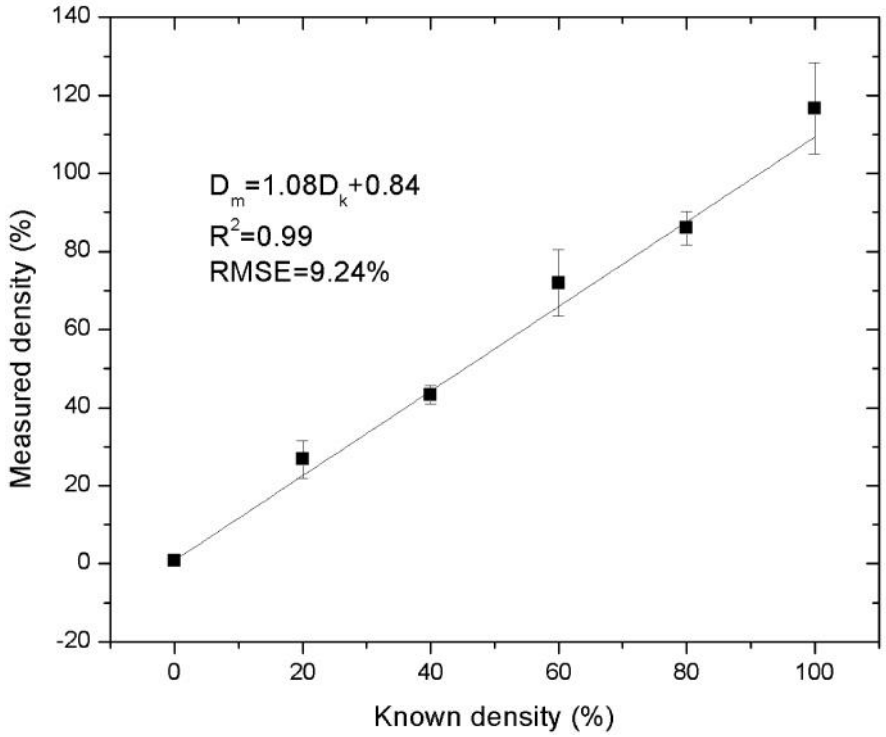

Figure 28: Plot of known and measured density of the inserted lesion disk phantoms

The density of the lesion phantoms were also measured and compared to known densities. This demonstrated a linear relation between the known and measured values and were represented by the equation $D_m=1.08D_k+0.84$ ($R^2=0.99$). An RMS error of 9.24% was calculated for the measured density (figure 28).

Discussion

The thickness of plastic water in the lesion phantoms could be measured with RMS error less than 1mm. A good linear relation with slope close to unity and very small offset was observed between the known and measured thicknesses.

In the case of adipose thickness measurement however, a large negative offset is observed. The measured thicknesses are all negative values. This may be attributed to presence of a large percentage of adipose in the surrounding breast tissue.

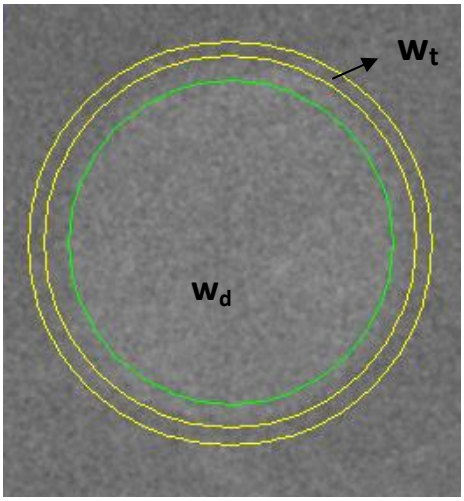

Figure 29: Lesion phantom with ROIs representing water thickness in specific columns of tissue

(a)

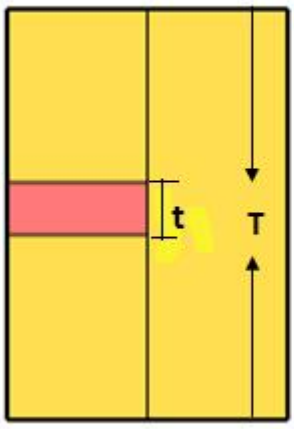

(b)

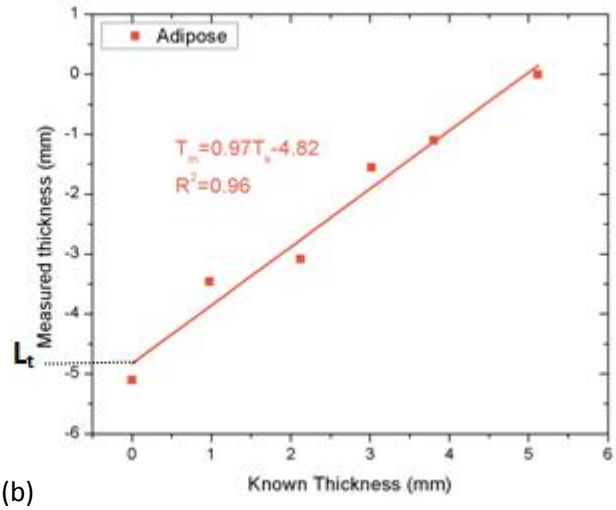

Figure 30: (a) Side view of the regions within the ROI (b) Adipose thickness plot

w_d corresponds to water in the lesion phantom disk of thickness *t=5mm* and the column of tissue above and below the disk. w_t is the water thickness in the column of tissue of thickness *T* immediately surrounding the lesion phantom. Since the percentage of water in the small region under consideration is negligible compared to the percentage of adipose in the breast tissue, w_t ~ 0 and hence there is no offset observed for plastic water thickness measurement. However, in case of adipose thickness, the offset is observed since the surrounding tissue contains higher percentage of adipose. Here, L_t, the thickness of adipose immediately surrounding the lesion phantom is ~t= 5mm. Thus approximately 5mm of offset, attributed but the surrounding adipose is observed.

Density could be measured with RMS error less than 10%. The errors in density estimation at each thickness level could mainly be due to different breast samples having different percentages of glandular and adipose, thereby offering different background noise. However, there existed good linear relation between the known and measured densities.

CHAPTER 7

Summary and conclusions

The results from this project indicate that dual-energy spectral mammography can be used to quantify the composition of breast tissue in terms of water and lipid for the purpose of stratifying patients based on breast cancer risk.

Further, the dual-energy material decomposition technique can be extended to lesion characterization, in order to classify breast lesions into benign and malignant based on water and lipid content. This may improve the predictive power for malignant lesions in screening mammography thereby reducing the number of false-positive cases.

Two-material calibration phantom was designed to have different densities of plastic water and adipose-equivalent plastic (chapter 4). The phantom was imaged with spectral mammography system and dual-energy material decomposition using a 3^{rd}-order function was performed to obtain the calibration coefficients. The coefficients were obtained over different tube voltages and thickness and density were measured and compared to known values. The small errors were indicative of a good agreement between the dataset and the fitting function applied thus, making it possible to apply these coefficients in the postmortem breast study to quantify water and lipid in the breasts.

For water and lipid quantification, conversion factors had to be developed in order to convert the plastic water and adipose thickness images to water and lipid thickness images (chapter 5). This was achieved through theoretical and experimental approaches. The obtained conversion

factors were then used to calculate the calibration coefficients for different thicknesses of water and lipid over different tube voltages. The application of the coefficients in the dual-energy decomposition equation along with the measured log-signal images resulted in water and lipid thickness images. The small errors in measured thickness and density in the calibration phase demonstrated that the conversion factors determined resulted in a good fit with the dataset and a good linear relation existed between the two.

The application of dual-energy decomposition was then extended to quantify the breast lesion materials (chapter 6). This involved imaging postmortem breasts with lesion phantom disks of known thicknesses and densities being inserted into them. The calibration coefficients obtained for plastic water and adipose-equivalent material (chapter 4) were applied along with the log-signal images in the dual-energy decomposition equation to obtain plastic water and adipose thickness images. The thickness and density of plastic water and adipose could be measured with small errors thereby demonstrating the capability of the technique in breast lesion material decomposition.

In conclusion, this project presents promising results that emphasize that dual-energy material decomposition using spectral mammography has the potential to quantify the chemical composition of breast tissue for the purpose of stratifying women based on breast cancer risk. It also illustrates encouraging results in quantifying the chemical composition of breast lesions to an accurate degree demonstrating the potential of lesion characterization to improve mammogram specificity.

Future work

The lesion phantoms inserted were uniform in size (0.5 cm total thickness and 2 cm diameter). Further analysis could be carried out to validate the technique by inserting lesion phantoms of different thicknesses and diameters.

The lesion phantoms were made of plastic water and adipose-equivalent plastic materials that are said to have X-ray attenuation properties similar to liquid water and adipose found in breast tissue. But, the adipose itself is a combination of 15% water and 85% lipid. Thus, these lesion phantoms might not exactly mimic water and lipid in the real breast lesions. The lesion phantoms could be replaced by bovine meat to help evaluate the technique better. This would not only provide the advantage of having lesions with real water and lipid but also resembles a real lesion in terms of its irregular shape. This could provide a better understanding of reliability of the dual-energy technique.

To further give a more realistic demonstration of the feasibility of lesion material quantification, lesions could be grown in mice. Once the lesions have grown to a suitable size they can be excised and inserted into the postmortem breasts for imaging and material quantification. The results from this study could prove to be very valuable in validating the dual-energy material decomposition technique for the purpose of breast lesion characterization.

The steps described until this stage demonstrates the feasibility of dual-energy spectral mammography in quantifying the chemical composition of breast tissue and breast lesions. The next stage would be to implement the actual characterization of lesions into benign and malignant based on the measured water and lipid in the breast lesions. Once this stage is

completed, patient studies could be carried out to evaluate the improvement in specificity of clinical mammography.

References

1. Howlader N, Noone AM, Krapcho M, Garshell J, Miller D, Altekruse SF, Kosary CL, Yu M, Ruhl J, TatalovichZ, Mariotto A, Lewis DR, Chen HS, Feuer EJ, Cronin KA (eds). SEER Cancer Statistics Review, 1975-2011, National Cancer Institute. Bethesda, MD, http://seer.cancer.gov/csr/1975_2011/, based on November 2013 SEER data submission, posted to the SEER web site, April 2014

2. Karellas, Andrew, and Srinivasan Vedantham. “Breast Cancer Imaging: A Perspective for the next Decade.” *Medical Physics* 35.11 (2008): 4878–4897.*PMC*. Web. 25 Apr. 2015.

3. Bellin M. F., Jakobsen J. A., Tomassin I., Thomsen H. S., Morcos S. K., Thomsen H. S., Morcos S. K., Almen T., Aspelin P., Bellin M. F., Clauss W., Flaten H., Grenier N., Idee J. M., Jakobsen J. A., Krestin G. P., Stacul F., and Webb J. A., “Contrast medium extravasation injury: Guidelines for prevention and management,” Eur. Radiol. 12(11), 2807–2812 (2002).

4. E.G. Olmstead, "Mammalian cell water; physiologic and clinical aspects," 1966

5. G. McIntyre, "Increased cell hydration promotes both tumor growth and metastasis: A biochemical mechanism consistent with genetic signatures," Medical hypotheses **69**, 1127-1130 (2007).

6. G. McIntyre, "Cell hydration as the primary factor in carcinogenesis: a unifying concept," Medical hypotheses **66**, 518-526 (2006).

7. S. Chung, A. Cerussi, C. Klifa, H. Baek, O. Birgul, G. Gulsen, S. Merritt, D. Hsiang, B. Tromberg, "In vivo water state measurements in breast cancer using broadband diffuse optical spectroscopy," Physics in medicine and biology **53**, 6713 (2008).

8. D. Hsiang, A. Durkin, J. Butler, B.J. Tromberg, A. Cerussi, N. Shah, "In vivo absorption, scattering, and physiologic properties of 58 malignant breast tumors determined by broadband diffuse optical spectroscopy," Journal of biomedical optics **11**, 044005-044005-044016 (2006).

9. Drukker, K., Duewer, F., Giger, M. L., Malkov, S., Flowers, C. I., Joe, B., Kerlikowske, K., Drukteinis, J. S., Li, H. and Shepherd, J., "Mammographic quantitative image analysis and biologic image composition for breast lesion characterization and classification" Med. Phys.41(3), March 2014

10. Taguchi, Katsuyuki, and Jan S. Iwanczyk. “Vision 20/20: Single Photon Counting X-Ray Detectors in Medical Imaging.” *Medical Physics* 40.10 (2013): 100901. *PMC*. Web. 12 Apr. 2015.

11. Le, Huy Q., Justin L. Ducote, and Sabee Molloi. “Radiation Dose Reduction Using a CdZnTe-Based Computed Tomography System: Comparison to Flat-Panel Detectors.” *Medical Physics* 37.3 (2010): 1225–1236. *PMC*. Web. 13 Apr. 2015.

12. Fujisaki T., Kimura M., Saitoh H., Abe S., and Hiraoka T., “Production design and evaluation of a novel breast phantom with various breast glandular fractions,” Radiat. Med. 24(10), 647–652 (2006).10.1007/s11604-006-0083 5 [PubMed] [Cross Ref]

13. E. Fredenberg, B. Svensson, M. Danielsson, B. Lazzari and B. Cederström, “Optimization of mammography with respect to anatomical noise”, in [Proc. SPIE, Physics of Medical Imaging], 7961, 796112(2011).

14. C. Bourgain& al. “A new technique for enhanced radiological-pathological correlation in breast cancer: multi-energy color X-ray”, RSNA Conference, Chicago, 2011.

15. Cahn, R.N., Cederström, B., Danielsson, M., Hall, A., Lundqvist, M., Nygrenn, D., 1999.Detective Quantum Efficiency dependence on X-ray energy weighting in Mammography. *Medical Physics,* 26(12), pp.2680-3.

16. Boyd NF, O’Sullivan B, Campbell JE, Fishell E, Simor I, et al. (1982) Mammographic signs as risk factors for breast cancer. Br J Cancer 45:185–193 doi: 10.1038/bjc.1982.327059469 [PMC free article][PubMed]

17. Harvey JA, Bovbjerg VE (2004) Quantitative assessment of mammographic density: relationship with breast cancer risk. Radiology 230:29–41 doi: 10.1148/radiol.230102087014617762 [PubMed]

18. Yaffe M (2008) Review: Measurement of Mammographic Density. Breast Cancer Research 10:209–219 doi: 10.1186/bcr210218598375 [PMC free article] [PubMed]

19. Blackmore, Kristina M. et al. “The Association between Breast Tissue Optical Content and Mammographic Density in Pre- and Post-Menopausal Women.” Ed. Yuan-Soon Ho. *PLoS ONE* 10.1 (2015): e0115851

20. P. R. Bevington, "*Data Reduction and Error Analysis for the Physical Sciences"*~McGraw-Hill, New York, NY, 1969.

21. S. Cheenu Kappadath and Chris C. Shaw, "Dual-energy digital mammography: Calibration and inverse-mapping techniques to estimate calcification thickness and glandular-tissue ratio" Medical Physics 30, 1110 (2003); doi: 10.1118/1.1576394.

22. K. Levenberg, "A method for the solution of certain problems in least squares," Quarterly of applied mathematics **2**, 164-168 (1944)

23. E. Schmitt, B. Threatt, "Effective breast cancer detection with film-screen mammography," Journal of the Canadian Association of Radiologists **36**, 304-307 (1985).

24. C.J. D'Orsi, "Early detection of breast cancer: mammography," Breast cancer research and treatment **18**, S107-S109 (1991).

25. J.M. Lewin, R.E. Hendrick, C.J. D'Orsi, P.K. Isaacs, L.J. Moss, A. Karellas, G.A. Sisney, C.C. Kuni, G.R. Cutter, "Comparison of Full-Field Digital Mammography with Screen-Film Mammography for Cancer Detection: Results of 4,945 Paired Examinations 1," Radiology **218**, 873-880 (2001).

26. M. Sala, M. Comas, F. Macià, J. Martinez, M. Casamitjana, X. Castells, "Implementation of digital mammography in a population-based breast cancer screening program: effect of screening round on recall rate and cancer detection," Radiology **252**, 31-39 (2009).

27. S. Chung, A. Cerussi, C. Klifa, H. Baek, O. Birgul, G. Gulsen, S. Merritt, D. Hsiang, B. Tromberg, "In vivo water state measurements in breast cancer using broadband diffuse optical spectroscopy," Physics in medicine and biology**53**, 6713 (2008).

28. D. Hsiang, A. Durkin, J. Butler, B.J. Tromberg, A. Cerussi, N. Shah, "In vivo absorption, scattering, and physiologic properties of 58 malignant breast tumors determined by broadband diffuse optical spectroscopy," Journal of biomedical optics **11**, 044005-044005-044016 (2006).

29. B.J. Tromberg, A. Cerussi, N. Shah, M. Compton, A. Durkin, D. Hsiang, J. Butler, R. Mehta, "Imaging in breast cancer: diffuse optics in breast cancer: detecting tumors in pre-menopausal women and monitoring neo adjuvant chemotherapy," Breast Cancer Research **7**, 279 (2005).

30. A.S. Haka, K.E. Shafer-Peltier, M. Fitzmaurice, J. Crowe, R.R. Dasari, M.S. Feld, "Diagnosing breast cancer by using Raman spectroscopy," Proceedings of the National Academy of Sciences of the United States of America **102**, 12371-12376 (2005).

31. E.G. Olmstead, "Mammalian cell water; physiologic and clinical aspects," 1966).

32. G. McIntyre, "Increased cell hydration promotes both tumor growth and metastasis: A biochemical mechanism consistent with genetic signatures," Medical hypotheses **69**, 1127-1130 (2007).

33. G. McIntyre, "Cell hydration as the primary factor in carcinogenesis: a unifying concept," Medical hypotheses **66**,518-526 (2006).

34. A.D. Laidevant, S. Malkov, C.I. Flowers, K. Kerlikowske, J.A. Shepherd, "Compositional breast imaging using a dual-energy mammography protocol," Medical physics **37**, 164-174 (2009).

35. J.L. Ducote, S. Molloi, "Quantification of breast density with dual energy mammography: A simulation study, "Med. Phys. **35**, 5411-5418 (2008).

36. J.L. Ducote, S. Molloi, "Quantification of breast density with dual energy mammography: An experimental feasibility study," Med. Phys. **37**, 793-801 (2010).

37. M. Aslund, B. Cederstrom, M. Lundqvist, M. Danielsson, "Physical characterization of a scanning photon counting digital mammography system based on Si-strip detectors," Med. Phys. **34**, 1918-1925 (2007).

38. H. Bornefalk, M. Hemmendorff, T. Hjärn, "Contrast-enhanced dual-energy mammography using a scanned multi slit system: evaluation of a differential beam filtering technique," Journal of Electronic Imaging **16**, 023006-023006-023007 (2007).

39. H. Bornefalk, J.M. Lewin, M. Danielsson, M. Lundqvist, "Single-shot dual-energy subtraction mammography with electronic spectrum splitting: Feasibility," European journal of radiology **60**, 275-278 (2006).

40. E. Fredenberg, M. Hemmendorff, B. Cederström, M. Åslund, M. Danielsson, "Contrast-enhanced spectral mammography with a photon-counting detector," Medical physics **37**, 2017-2029 (2010).

41. E. Fredenberg, M. Lundqvist, B. Cederstrom, M. Aslund, M. Danielsson, "Energy resolution of a photon-counting silicon strip detector," Nuclear Instruments & Methods in Physics Research Section a-Accelerators Spectrometers Detectors and Associated Equipment **613**, 156-162 (2010).

42. H. Ding, J.L. Ducote, S. Molloi, "Breast composition measurement with a cadmium-zinc-telluride based spectral computed tomography system," Medical physics **39**, 1289-1297 (2012).

43. H.Q. Woodard, D.R. White, "The Composition of Body-Tissues," British Journal of Radiology **59**, 1209-1219(1986).

44. L. Alfonso R., D. Huanjun , M. Sabee, "Quantification of breast density using dual-energy mammography with liquid phantom calibration," Physics in medicine and biology Accepted(2014).